FINAL REPORT

COVER PAGE

Federal Agency to which Report is submitted: DOE EERE – Wind & Water Power Program

Recipient: UCAR, DUNS Number: 078339587
Award Number: DE-EE0005374
Project Title: Investigating Marine Boundary Layer Parameterizations by Combining Observations with Models via State Estimation
Project Period: April 16, 2013 to April 15, 2015

Principle Investigator (PI): Luca Delle Monache, Dr., lucadm@ucar.edu, (303) 497-2736
Report Submitted by: PI

Date of Report: June 30, 2015

Working Partners:
Dr. Andrew Clifton (Co-PI, NREL), Andrew.Clifton@nrel.gov
Dr. Josh Hacker (Co-PI, NCAR), hacker@ucar.edu
Dr. Branko Kosovic (Co-I, NCAR), branko@ucar.edu
Dr. Jared Lee (Co-I, NCAR), jaredlee@ucar.edu
Dr. Francois Vandenberghe (Co-PI, NCAR), vandenb@ucar.edu
Dr. Yonghui Wu (Co-I, NCAR), yonghuiw@ucar.edu

Cost-Sharing Partners:
Dr. Sam Hawkins (Co-I, Vattenfall), sam.hawkins@vattenfall.com
Dr. Jesper Nissen (Co-I, Vattenfall), jespernielsen.nissen@vattenfall.com

DOE Project Team: DOE HQ Program Manager – Jose Zayas
DOE Field Contract Officer – Laura Merrick
DOE Field Grants Management Specialist – Jane Sanders
DOE Field Project Officer – Michael Hahn
DOE/CNJV Project Monitor – Andrew Buckspan

Signature of Submitting Official: ___ ___________________

ACCOMPLISHMENTS

PROJECT OBJECTIVE

The outcome of this project is an improved understanding of the complex interactions between the atmosphere and the ocean surface. This knowledge will be used to develop improved marine boundary layer (MBL) parameterizations, as well as improved ocean-atmospheric coupling techniques, significantly reducing market barriers to offshore wind energy, delivering the Department of Energy's goals.

PROJECT GOALS

- More accurate predictions of turbine hub-height winds in marine environments, resulting in improved power prediction and potentially saving millions of dollars for the wind energy industry;
- Improved wind resource assessment techniques in marine environments.

As described in detail in the next sections, **the goals of improving predictions of turbine hub-height winds in marine environments has been achieved**.

The results and description of the techniques developed will be submitted for publication in the open peer-reviewed literature and will be shared with the scientific and U.S. off-shore wind energy industry communities via community codes and models.

GOAL STATUS

Progress and updates for each of the tasks is reported next, including major activities, specific objectives; significant results including major findings, developments, or conclusions; key outcomes, milestones, and other achievements.

TABLE OF CONTENTS

Introduction 5

1. Collection of observational data sets, quality control, formatting, and analysis 7

2. Implementation of 2-way coupling between WRF SCM and WWIII 15

3. State Estimation (SE) Experiments with WRF SCM/DART 21

Summary and Conclusions 45

Introduction

The atmospheric boundary layer (ABL) spatial and temporal evolution is driven by the coupling of the atmosphere to the surface via fluxes of heat and momentum. Typically, in numerical weather prediction (NWP) models these fluxes are estimated from the available mean quantities. A powerful set of statistical relationship was derived from Monin-Obukhov similarity theory (MOST; Lumley and Panofsky 1964; Wyngaard 1973) based on pioneering field campaigns held in the 1960s and 1970s (e.g., 1968 Kansas, Izumi 1971); the latter sought to improve our understanding of the turbulence characteristics in the atmospheric surface layer, i.e., the ABL portion closest to the ground. Currently, MOST is still the basis of state-of-the-science NWP model surface layer formulations. However, the universality of its relationships is questionable when applied offshore, given that its formulation is based on (incomplete) land-based measurements. Indeed, several past studies have found evidence of MOST deficiencies when it is applied to marine boundary layer (MBL, e.g., Geernaert et al. 1986; Rieder et al. 1994; Donelan et al. 1993; and Hare et al. 1997; Edson and Fairall 1998; Sjöblom and Smedman 2002, 2003; Smedman et al. 2003, 2009; Pichugina et al. 2011).

Obukhov (1946) and Monin and Obukhov (1954) formulated their similarity hypothesis on the statistical nature of the turbulent flow based on the relationship between mechanical and thermal forcing in the surface layer. In MOST, the structure of the turbulent flow is determined by the height above the surface (z), buoyancy ($g/\overline{\Theta}_v$), friction velocity (u_*), and surface vertical buoyancy flux ($\overline{w\theta}_{v0}$), where $\overline{\Theta}_v$ is the virtual potential temperature and g is the acceleration due to gravity (Wyngaard 1973). Both u_* and $\overline{w\theta}_{v0}$ can be expressed as function of the surface stress and heat flux:

$$u_* = \sqrt{\frac{|\tau_0|}{\rho}} \quad (1), \text{ and } \quad \overline{w\theta}_{v0} = \frac{Q_0}{\rho c_p} + 0.61 T_0 \frac{E_o}{\rho L_e} \quad (2)$$

where τ_0 is the surface stress vector (i.e., the surface value of the momentum flux), Q_0, T_0, and E_o are the surface values of the sensible heat flux, temperature, and latent heat flux, respectively, ρ is the air density, c_p is the specific heat at constant pressure, and L_e is the latent heat of vaporization of water. In the surface layer, fluxes are assumed constant with height (z).

A proper treatment of the MBL requires additional scaling parameters to account for the momentum production and dissipation generated by the highly variable ocean waves (Sullivan et al. 2008). Recently, Hanley and Belcher (2008) found that ocean wave momentum flux can affect the entire MBL wind profile. Following Edson and Fairall (1998), we can define a wave boundary layer (WBL), which is the portion of the surface layer in the MBL where the ocean wave contribution to the turbulence budget is present. In the WBL the momentum equation can be written as follows:

$$\frac{\partial}{\partial z}\left(-\overline{\tilde{u}\tilde{v}} - \overline{u'v'} + v\frac{\partial \overline{U}}{z}\right) \approx 0 \quad (3)$$

where primes are fluctuations around the mean value ($\overline{U}$), tildes denote wave induced fluctuations, and v is the kinematic viscosity. In this study we propose to improve models representation of the MBL lower-level winds.

Observations of key quantities in Eqs. (1)-(3) are very limited (Smedman et al. 2009), and when available, they are sparse in time and space (Pichugina et al. 2011). State estimation (SE) provides a theoretically optimal framework for combining observations and numerical simulations, filling the gaps in the observational data sets with model estimates. As described in detail in the next section, the SE allows new insights into model dynamics and errors. If implemented properly, very-short-range predictions (minutes to hours) skillfully predict the future atmospheric state. The model, then, is representing the state of the system, here a coupled atmosphere-ocean surface, with the greatest fidelity achievable for the model given a set of observations. It can then be interrogated for internal balances, budgets, and error structures.

The main tools implemented in this project to explore and improve the performance of current modeling capabilities in the MBL include:

- The National Center for Atmospheric Research (NCAR) Weather and Research Forecasting model, WRF, both in his single column (SCM) and three-dimensional (3D) versions;
- The National Oceanic and Atmospheric Administration (NOAA) Wave Watch III (WWIII);
- SE algorithms from the Data Assimilation Research Testbed (DART, Anderson et al. 2009);
- Observations of key quantities of the lower MBL, including temperature and winds at multiple levels above the sea surface.

The following sections include a description of the data sets used in these studies, the coupling of the weather model WRF and wave model WWIII, the SE experiments with WRF SCM and 3D coupled with the DART system, and a summary and conclusions.

1. Collection of observational data sets, quality control, formatting, and analysis

The following are the main steps of this task:

- Selection of location/data sets suitable for the state estimation (SE) experiments;
- Performance of a preliminary analysis of the atmospheric stability conditions at the selected location;
- Selection of periods when conditions were neutral or slightly convective, which are the conditions sought for the SE experiments;
- Conversion of the observations for the selected period in the input format for the Data Assimilation Research Testbed (DART).

1.1 Selection of location/data sets for the SE experiments

For this task we were able to make leverage (i.e., avoid duplicated efforts) on the analysis that have been already performed by Patton et al., whose project has been awarded under the same DOE call. Patton et al. considered a variety of field campaigns, observing platforms and locations as candidate sites/data sets to study the interactions between the lower atmosphere and the sea state. Their throughout analysis resulted in the selection of the FINO 1 data sets for the year of 2006, which is described in details below.

FINO 1 is an approximately 80-m tower mounted on a platform 20 m above the mean sea level, giving measurements of atmospheric conditions at multiple levels to approximately 100 m above sea level (Figure 1.1). The platform is approximately 50 km North East of Emden, Germany, in the North Sea. FINO 1 was built partly to quantify the wind characteristics before the Alpha Ventus wind plant was built. Construction of the Alpha Ventus started with the installation of the substation in July 2008. This analysis therefore uses data from 2006, when the winds measured at the site represent the undisturbed flow. The analysis could be extended if required. Historic data from the platform instrumentation are accessed through the FINO database at http://fino.bsh.de using Co-PI Clifton's credentials. Permission has been given by the German Department for Shipping and Hydrography to share data with the project members for this project only.

A variety of data are collected at different heights on the tower (Tables 1.1 and 1.2). There is only a single cup anemometer and wind vane at each level on the tower, and booms are a similar length to the tower face width (Figure 1.2). This means that the wind speed measurements are potentially impacted by flow speeding up or slowing down around the tower structure. The cup anemometers are mounted on booms that extend in the direction 127°-135°; therefore, when winds are from 310° ± 30°, wind speed measurements should be considered potentially impacted by wakes from the tower structure.

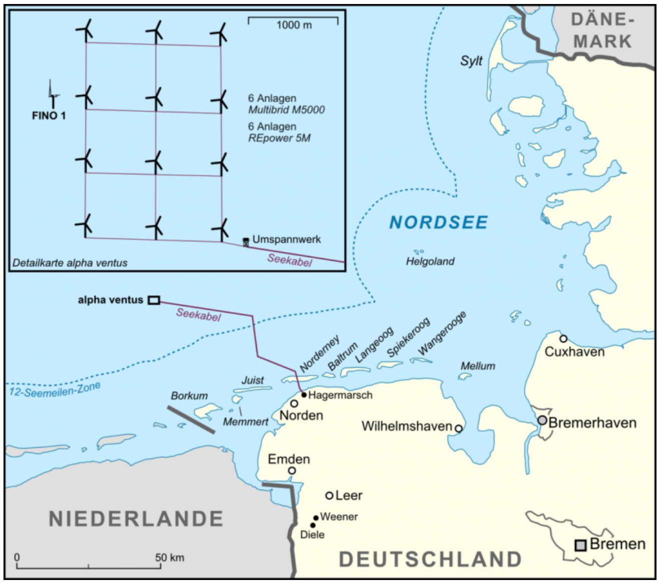

a) Location of the FINO 1 platform in the North Sea

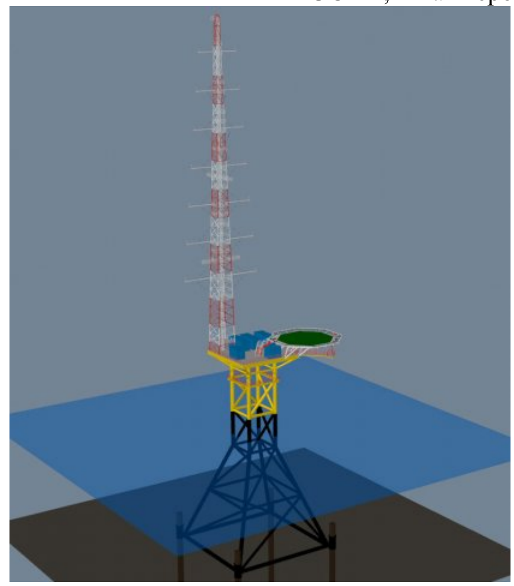

b) FINO 1 platform

Figure 1.1 Location and configuration of the FINO 1 platform. Images are from www.fino1de.

Table 1.1 Instrumentation heights. Heights are given with respect to the Lowest Astronomical tide (LAT).

Elevation [m]	Parameter(s)
103	WS, AT, RH
91.5	WS, WD
81.5	WS
71.5	WS, WD, AT
61.5	WS
51.5	WS, WD, AT, RH
41.5	WS
34	WS, WD, AT, RH
20 (deck)	AP, Precip

Table 1.2 Instrumentation installed on the FINO 1 platform.

Parameter	Description	Device
WD	Wind direction	Thies wind vane
WS	Wind speed	Vector cup anemometer
AT	Temperature	Thies 100 ohm PRT
AP	Air pressure	Vaisala capacitance sensor
RH	Relative humidity	Hair-tension hygrometer
Precip	Precipitation rate	Thies optical sensor

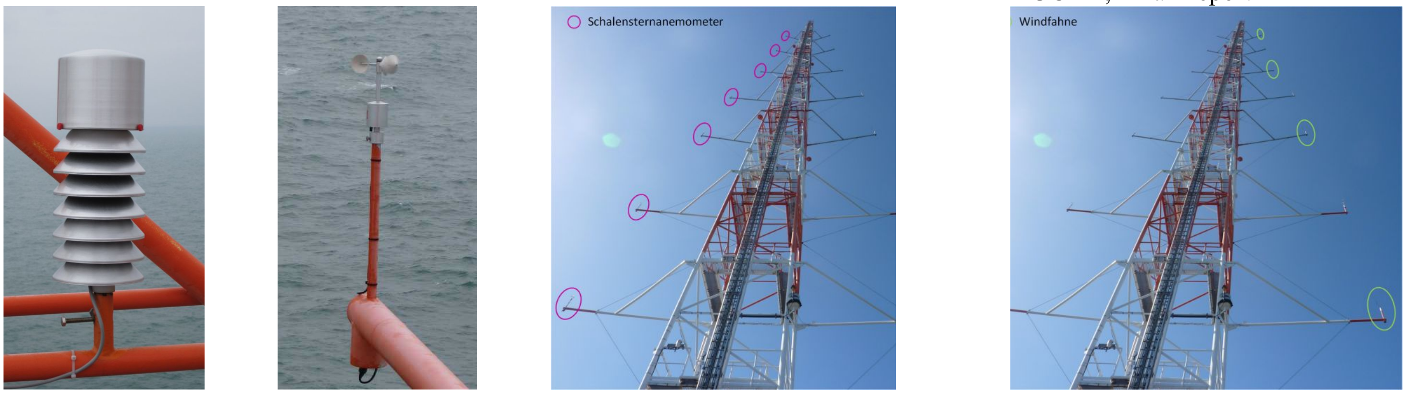

a) Temperature sensors b) Cup anemometers c) Positions of cup anemometers (circled) d) Positions of wind vanes (circled)

Figure 1.2 Instrument mountings on the FINO 1 Platform

2.2 Analysis of wind climatology and atmospheric stability conditions at FINO 1

Time series of wind speeds for the year 2006 are presented in Figure 1.3. Windier months are observed from October to December, whereas June, July and August are the months were lighter winds were observed.

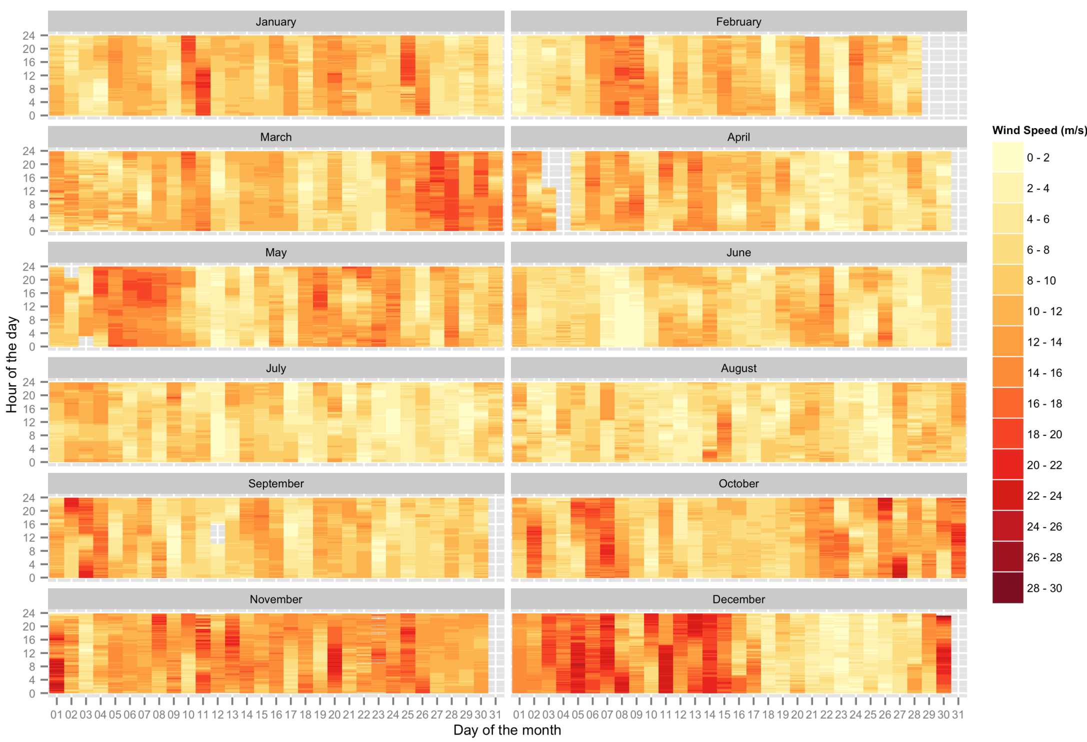

Figure 1.3 Time series of 10-minute mean wind speed at 81.5 m above LAT. Data are from 2006.

Atmospheric stability is a combination of static and dynamic stability. Static stability is the "ability of a fluid at rest to become turbulent or laminar as a result of buoyancy". Dynamic stability is "a measure of the ability of a fluid to resist or recover from finite perturbations of a steady state" (Glickman 2000). So, atmospheric stability can change depending on the wind speed and thermodynamic profile of the atmospheric boundary layer. A stable atmosphere resists motion, which suppresses turbulence. In contrast, an unstable atmosphere has enhanced turbulence. In a neutral atmosphere, the boundary layer temperature profile follows the adiabatic lapse rate and the wind speed follows the logarithmic (constant shear) wind profile.
The gradient Richardson Number quantifies atmospheric stability, using the ratio of the wind speed gradient to the buoyancy gradient:

$$Ri = \frac{g}{T_v} \cdot \frac{d\theta_v / dz}{\left[dU / dz \right]^2}$$

where g is the acceleration due to gravity, $d\Theta_v/dz$ is the virtual potential temperature gradient through the boundary layer, T_v is the mean virtual temperature, and dU/dz is the wind speed gradient[1]. The virtual temperature is a function of dry-air temperature and humidity, while the virtual potential temperature is a function of height, pressure, dry-air temperature and humidity. The wind speed U is the average wind speed measured by the cup anemometers. In this case, data are averaged over 10 minutes to give a representative state of the atmospheric boundary layer (ABL) in that interval.

The time series of Richardson Number from the platform deck to 100 m above LAT at FINO 1 is plotted in Figure 1.4. Data have not been filtered to remove wind directions where the cup anemometers may be shadowed. Positive values of Ri indicate that the atmosphere is stably stratified. Negative values indicate that the atmosphere is unstable. Richardson numbers with a magnitude less than 0.01 indicate neutral conditions. Plotting the distribution of stability by month (Figure 1.5) shows that the ABL at the FINO1 platform from neutral to unstable from August through March, while April through July tends to be stable. The conditions searched for this study, neutral and slightly convective, are often observed for the months of January, February, October, November, and December. This seasonal trend suggests that stability at this location is strongly dependent on the temperature of the water compared to the atmosphere, as during winter the water is likely to be warmer than the air, leading to unstable conditions. During the summer, the water is likely cooler, leading to stable conditions. Although the water surface temperature is available at this site, it was not investigated as part of this study.

Atmospheric stability at the FINO 1 location shows a slight relationship to wind speed (Figure 1.6). In that figure, data have been categorized according to ranges of stability that are typically used for the ABL:

---

[1] Ideally $\left[\frac{du}{dz}\right]^2 + \left[\frac{dv}{dz}\right]^2$, where u and v are the meridional and zonal wind components, would be used instead of $\left[\frac{dU}{dz}\right]^2$. However, the wind direction data at the FINO 1 platform are not reliable and this version is used instead.

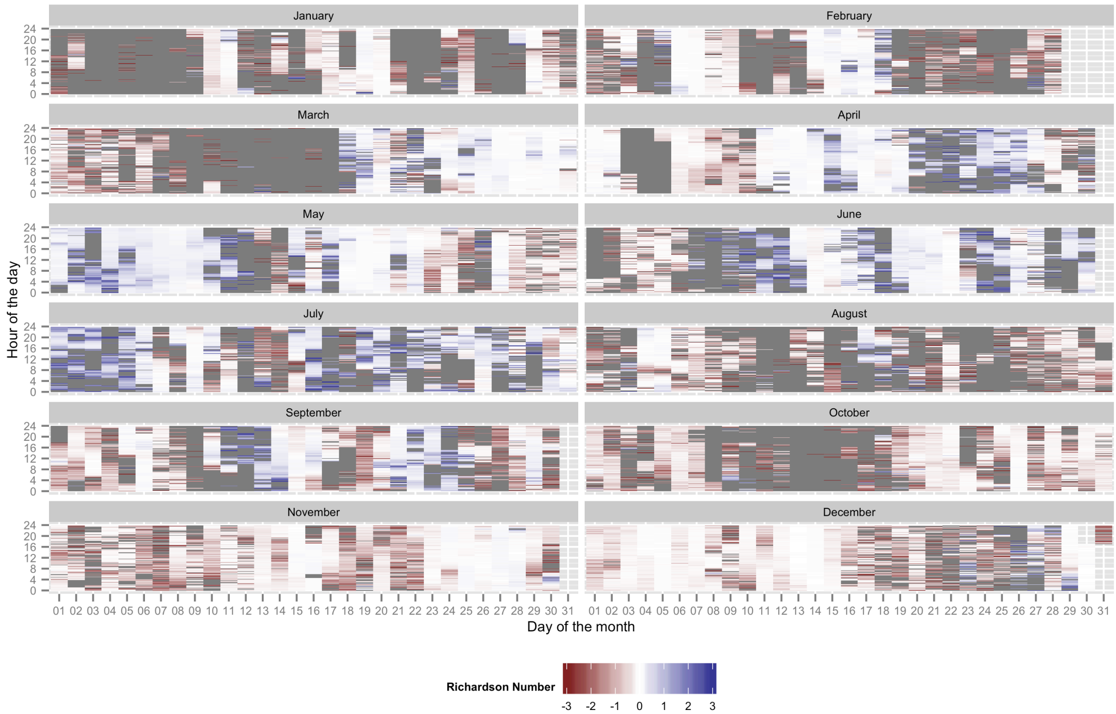

Figure 1.4 Time series of Gradient Richardson Number. Data are 10-minute values, colored according to the scale at the bottom. Grey areas indicate intervals where the data required for the calculation were not available. Data have not been filtered by direction or wind speed.

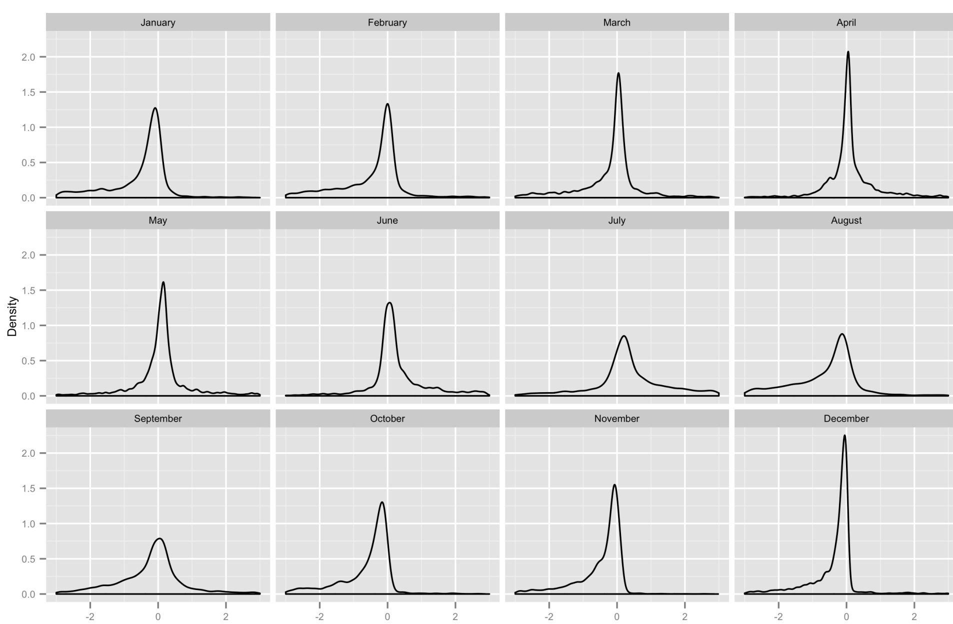

Figure 1.5 Monthly distribution of Gradient Richardson Number at the FINO1 platform. Data have not been filtered by wind speed or direction.

- Strongly stable: Ri > 0.25;
- Stable: 0.01 < Ri < 0.25;
- Neutral: -0.01< Ri < 0.01;
- Unstable: -10 < Ri < -0.01;
- Strongly unstable: Ri < -10.

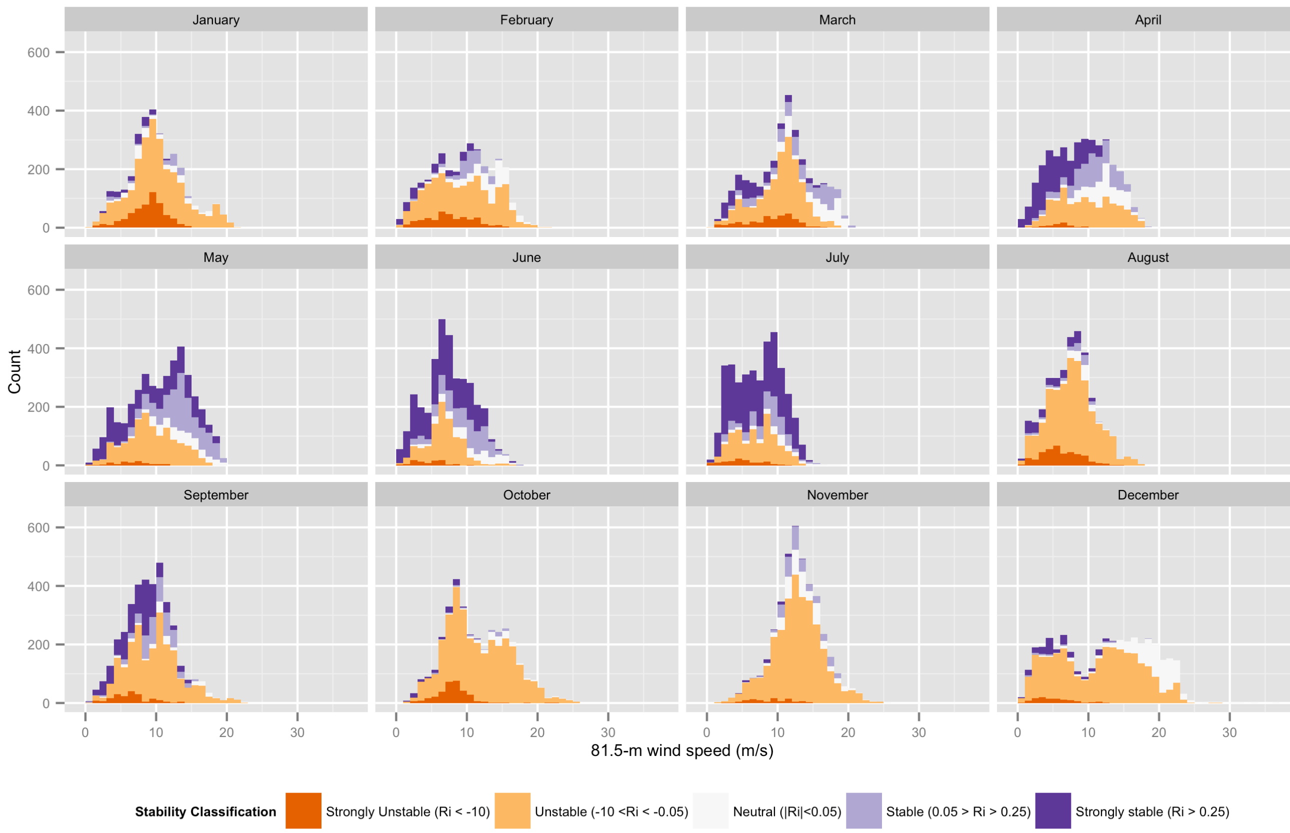

Figure 1.6 Monthly distributions of wind speed and stability. Stability data are plotted as a function of the 81.5 m wind speed.

Neutral conditions are most often seen in February, March, April and December when wind speeds exceed 5 m/s. These wind speeds imply that there is significant upwind heat transfer between the water surface and the atmosphere such that they are able to achieve thermal equilibrium and thus reduce the heat transfer at the FINO 1 location. Also, at this time of year there may not be a large difference in temperature between the air and sea surface, making it easier to achieve equilibrium conditions.

A goal of this study was to identify when conditions were neutral for or slightly convective. The time series of binned Richardson number is plotted in Figure 1.7, from which it can be seen that there are several periods when the ABL was neutral for 24 hours or more. These occurred on February 6-7, Mar 28, December 5, 13-15, and 30.

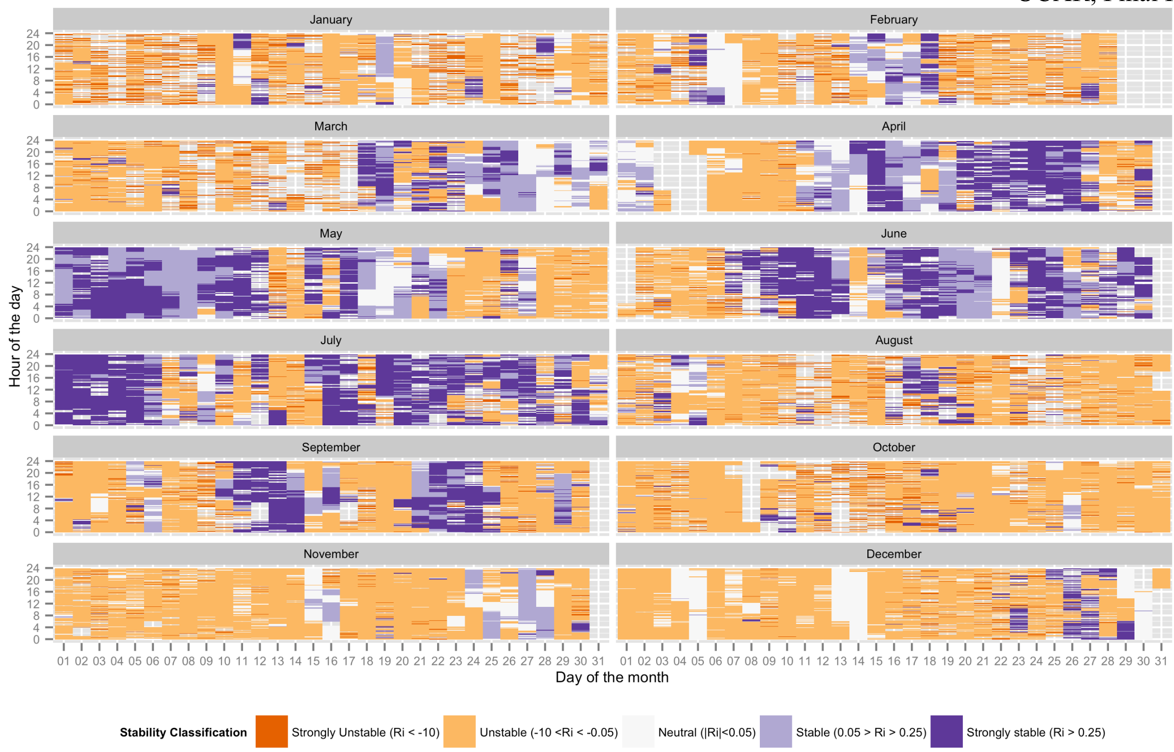

Figure 1.7 Time series of stability class. Data are 10-minute Richardson number binned according to the scale at the bottom of the plot. Grey areas indicate intervals where the data required for the calculation were not available. Data have not been filtered by direction or wind speed.

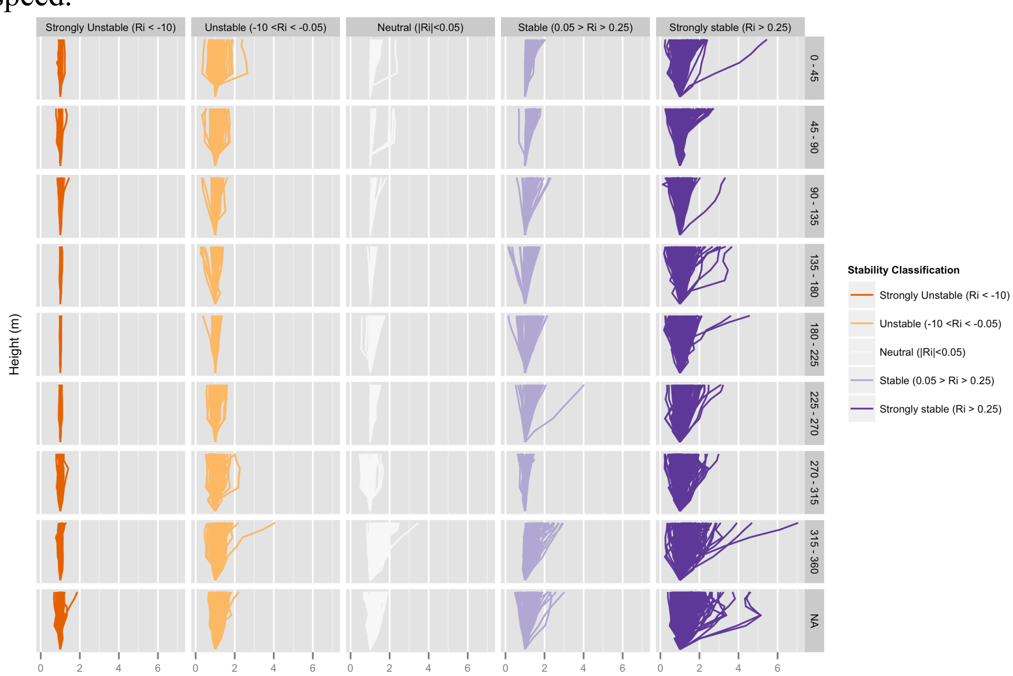

Figure 1.8 Wind profiles for different stability regimes. Wind speeds are normalized by the wind speed at the lowest level (33 m above LAT) and grouped according to wind direction at 80 m above LAT. 'NA' indicates that the wind direction measurement failed.

Wind profiles for different stability regimes and different wind directions are plotted in Figure 1.8. Data are normalized by the wind speed at the lowest measurement height (33 m above LAT) to more clearly show the variation in wind speed with height. Profiles are similar to what would be expected from theory; in unstable conditions, there is little variation of wind speed with height, while stable conditions show a steeper, positive gradient to the wind speed.

1.3 Selection of periods suitable for the SE experiments

Based on the results above, and the desirability for the SE experiments to have continuous simulation periods, the selected periods of year 2006 at FINO 1 include the months of January, February, October, November, and December.

1.4 Conversion of the observations for the selected period in the input format for DART

The available observation data sets over the selected period have been converted to a format suitable to the tools and software available as part of the DART capabilities, which are freely available to the broader community.

1.5 Additional data sets

Additional data sets used in the studies and analysis described in the following sections include:

- The NOAA Meteorological Assimilation Data Ingest System (MADIS) data stream over the domain of interest. MADIS includes data in real-time from several platforms, as surface stations, radiosondes, aircraft reports, buoys, etc.
- The World Meteorological Organization (WMO) Global Telecommunications Service (GTS) database (http://www.wmo.int/pages/prog/www/TEM/index_en.html). Those are worldwide observations made available in real-time by NOAA.

2. Implementation of 2-way coupling between WRF SCM and WWIII

2.1 Background

In a previous effort, NCAR has coupled the community models WRF (atmosphere) and NOAA's WWIII (wave). The coupling was "1 way" in which hourly 10-meter winds and sea ice from the WRF model are used to force the WWIII model. Since both models support nesting, it was possible to downscale information for both wind and ocean waves down to the kilometer scale. The 1-way coupling was completed in 2010 with WRF version 3.1 and WWIII version 3.14.

The objective of this new effort was to couple "2 ways" the two models so that the WWIII roughness length (ZNT) can be passed as boundary forcing to WRF, while WRF 10-meter wind U10 and V10 and sea ice fields are passed to force WWIII. The roughness length in WRF is primarily function of land cover. The vegetation at a given grid point is read from a monthly table, together with a minimal and maximal value ZNT that is typical for the corresponding vegetation type. Over water the minimum and maximum are the same and equal to 0.0001m. Therefore, there is no spatial and temporal variation over water in WRF. Similarly, in absence of reliable data, sea ice always is set to 0 in WRF. See details at http://www2.mmm.ucar.edu/wrf/users/docs/user_guide_V3/users_guide_chap5.htm . There are currently four schemes to compute the roughness length in WWIII: a simple derivation from the 10-m wind (option FLX1, Wu 1980) and thee more sophisticated schemes, based on friction velocity. See details in http://polar.ncep.noaa.gov/waves/wavewatch/manual.v4.18.pdf . Two of the schemes (FLX2 and FLX3) are based on Tolman and Chalikov (1996) formulation. The third option (FLX3) is a variation of option 2 (FLX2), but the drag coefficient is capped. The fourth option (FLX4) is based on Hwang (2011) formulation. Compared, to FLX2 and FLX3, it includes a threshold on the 10-m wind speed, below which the drag coefficient remains constant. This prevents the drag coefficient from dropping to 0.

At the time when this effort began (July 2013), WRF version 3.5.1 was just about to come out. Similarly, a new global reanalysis data set: the Climate Forecast Reanalysis System (http://cfs.ncep.noaa.gov/cfsr/) had been made available to the community. This data set which provides 6-hourly global reanalysis at 0.5° from 1979 to present is a significant improvement with respect to the reanalysis used in the "1-way" coupling effort. The latter used the NCEP/NCAR Reanalysis Project (NNRP) at 2.5°. Consequently, the work began by upgrading the "1-way" existing coupled system with WRF version 3.5.1 forced by the CFSR global data set. In March 2014, NOAA released to the public version 4.18 of WWIII. This new version has many new features and improvements compared to version 3.14 (see http://polar.ncep.noaa.gov/waves/wavewatch/ for an exhaustive list). Although the work on "2-way" coupling version 3.14 had already started for several months at the time of the release, it was decided to adopt version 4.18 to keep the modeling system up to dare. This version is still the official WWIII release as of June 2015.

2.2 Coupling strategy

WRF and WWIII are fully parallelized computer code to efficiently run on multi-core computers. The parallelization of each code is, however, very different. WRF is based on a domain decomposition, i.e., the WRF horizontal domain is divided into as many geographic sub-domains as there are processors and each sub-domain is integrated on one single processor exchanging information on the boundaries with its neighbors. The WWIII parallelization is not based on geography but instead distribute the wave spectrum across processors. Because of the complication due to the different parallelization paradigms of the model and the limited time and resources allowed to the task, an approach in which models are coupled through file exchange was preferred. Numerically, this approach can be less efficient than coupling through computer memory, but physically it can be justified by the fact that 10-m winds and roughness length vary on time scale much larger than the models time steps (e.g., ~15 s for the WRF domain with 3 Km grid increments). Therefore, the exchange of information at the interface of the two models can be done at frequencies that allow the use of files. Typically, we have used 1 hour as our coupling frequency. This is to say, that information is exchanged between the two models every hour. So, 10-m wind and roughness length are varying hourly when apply as forcing in, respectively, WWIII and WRF. However, the system we have built can easily be extended for higher frequency exchanges between the atmosphere and wave models by changing an input parameter.

Nesting applies differently according to the physics of the atmosphere and ocean. Through WRF nested domains, coarse (from 0.5° to 2.5° depending on global models) global fields are successively downscaled to 30 km, 10 km and 3.3 km grid increments. However, there are no global wave analyses publicly available; therefore, the first WWIII domain must be global. In addition a ratio of 10, compared to 3 with WRF, can be applied when nesting domains with WWIII. Consequently, only surface winds from WRF two innermost domains are used to drive WWIII and the CFSR global data are used to force WWIII on the global outer domain. Table 2.1 illustrates the WRF and WWIII nested domains and the interactions between the atmospheric and wave models for each domain.

Atmosphere		Wave
Δx = 1/2° global Δx = 30km regional	U10, V10 ZNT	Δx = 1/3° global
Δx = 10km regional	U10, V10 ZNT	Δx = 1/10° regional
Δx = 3.3km regional	U10, V10 ZNT	Δx = 1/30° regional

Table 2.1: WRF and WWIII nested domains grid increment and the model variables exchanged on each domain during the 2-way coupled runs.

The two innermost WWIII domains had been defined to match WRF inner domains. Figure 2.1 shows WRF domain 1 (leftmost panel) in the nested configuration with the two nested subdomains common to WRF and WWIII. WWIII domain 1 is global at 1/3° increment.

The the following are the main steps of the coupling algorithm:

For each hour ***t***:

1) Interpolate CFSR 1/2° U10(t) & V10(t) onto WWIII 1/3° global grid
2) Interpolate WRF 10km U10(t) & V10(t) onto WWIII 1/10° grid
3) Interpolate WRF 3.3km U10(t) & V10(t) onto WWIII 1/30° grid
4) Save data in WWIII input file
5) Run WWII between ***t*** and ***t+1hr***
6) Interpolate WWIII 1/3° ZNT(t+1) onto WRF 30km grid

7) Interpolate WWIII 1/10° ZNT(t+1) onto WRF 10km grid
8) Interpolate WWIII 1/30° ZNT(t+1) onto WRF 3.3km grid
9) Save data in WRF auxiliary file
10) Run WWII between ***t*** and ***t+1hr***

The restart capability is used every hour for both WRF and WWIII. The ZNT variable after interpolation onto the WRF grids is passed through WRF auxiliary input files.

2.3 Code changes and scripting
Changes were needed in both WRF and WWIII code. We added into WRF registry the definition of a new 2-dimensional field ZNT_WW3 that is read and written out through the WRF auxiliary file functionality. This changes result in WRF automatically loading the roughness length field from WWIII after interpolation onto the WRF grids and reformatting to the WRF standard I/O. In WRF main driver (routine *module_first_rk_step_part1.F*), changes were needed to pass the information into the routine handling the physics at the surface. In WRF surface scheme's main driver (routine *module_sf_mynn.F* in our experiments) changes were made to assure that the roughness length that was passed wasn't overwritten. Changes in the WWIII code were more complex. Since we wanted to use the FLX2 option, we had to firstly modify the *Gridgen* packages so that the fluxes between the mother domain and nested domain can be exchanged. *Gridgen* is the utility that builds the WWIII grids with bathymetry. Secondly, we modified the code so that the roughness length field can be outputted (routines w3wavemd.ftn, w3iogomd.ftn, w3srcemd.ftn). Finally, we had to fix what seems to be a bug in WWIII version V4.18, so that the roughness length field from the immediate sub-domain is not embedded in the mother domain field when written out (routine ww3_ounf.ftn).

Scripts were written to drive the coupled system. A master script allows conducting a simulation with only the starting date, ending date and the coupling frequency as input parameters. All the WRF input and boundary files for the entire simulation period must have been generated beforehand. The user can select the coupling mode (1-way or 2-way). The script assumes that a restart file for both WRF and WWIII are available at initial time.

2.4 Performances
The I/O overhead that results from coupling using hourly files slows down the runs of about 15% on 256 processors. Table 2.2 shows the overhead in percent of the wall-clock time as function of the number of processors. The overhead is defined as the time spent on writing and reading the files, as well as the interpolations, divided by the sum of the wall clock time of each model.

Number of processors 2.6-GHz Intel Xeon E5-2670 (Sandy Bridge)	Overhead in % of wall-clock time
16	4%
64	10%
256	15%

Table 2.2: Overhead in percent of wall clock time as function of the number of processors.

Since both WRF and WWIII are parallelized and ran faster as the number of processors increases, while the operations (interpolation, formatting, etc.) needed to generate the files at the interface of the two models are serial, the overhead increases with the number of processors.

2.5 Numerical experiments

The coupled system was applied to the FINO1 tower case over the months of July and October 2006. Three nested domains were used for both WRF and WWIII. Table 3 provides the grid size and grid increment for all domains.

WRF	WWIII
132x132 points at 30 km	720x315 points at 1/3° (global)
132x132 points at 10 km	157x103 points at 1/10°
132x132 points at 3.3 km	175x109 points at 1/30°

Table 3: WRF and WWIII dimensions and grid increment.

There were 51 vertical levels in WRF. The first lower 10 levels were located at 12 m, 32 m, 48 m, 63 m, 79 m, 99 m, 123 m and 147 m, 179 m and 219 m above ground level, which corresponds to sea level at the FINO1 tower location. The Thompson Physics, MYNN Planetary Boundary Layer, Kain Fritsh Cumulus parametrization (first two coarser domains only), NOAH land surface model and RRTM / Dudhia radiation schemes were used. The lateral and initial conditions were provided by the 6-houry 1/2° Climate Forecast Reanalysis System global data set. The 1/12° (~10 km) sea surface temperature from NCEP Real Time Global products (http://polar.ncep.noaa.gov/sst/) was applied on the coarsest domain, while sea 1/30° (~4 km) surface temperature from the Danish Meteorological Institute (DMI) was applied on the other two domains. DMI SST data are available from the European MyOcean server. Figure 2.1 shows the WRF domain configurations and Figure 2.2 overlays the DMI regional SST data over the WRF domain 1.

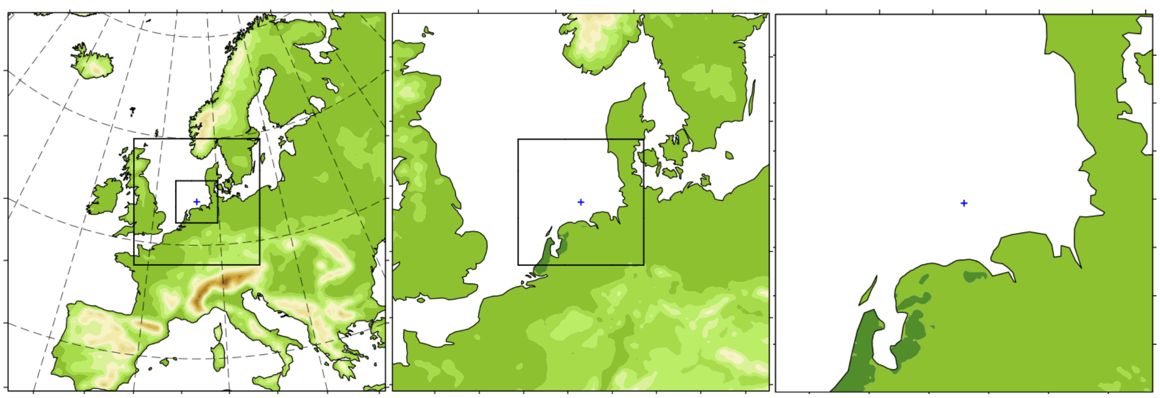

Figure 2.1 WRF nested domains configuration

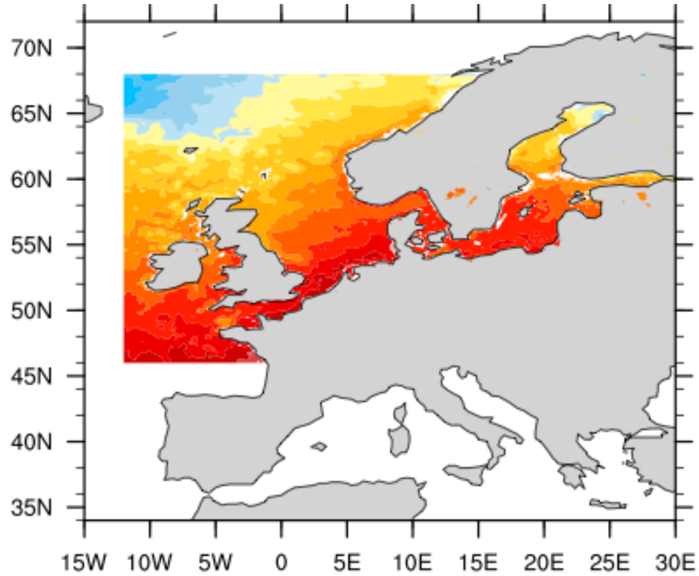

Figure 2.2 regional 1/30° SST data from DMI overlaid on WRF domain 1.

Figure 2.3 presents the 10-m wind for WRF domain 2 and 3 at 01z on July 2, 2006. Figure 2.4 depicts the roughness length from WRF on domain 1 at 01z on July 2, 2006 in absence of coupling. Figure 2.5 shows the roughness length from WWIII on domain 2 (left panel) and domain 3 (right panel) at 01z on July 2, 2006. The roughness lengths on Figure 2.5 have been scaled by 10^5 for readability over water. The WRF roughness length on Figure 2.4 is constant over sea equal to 0.0001.

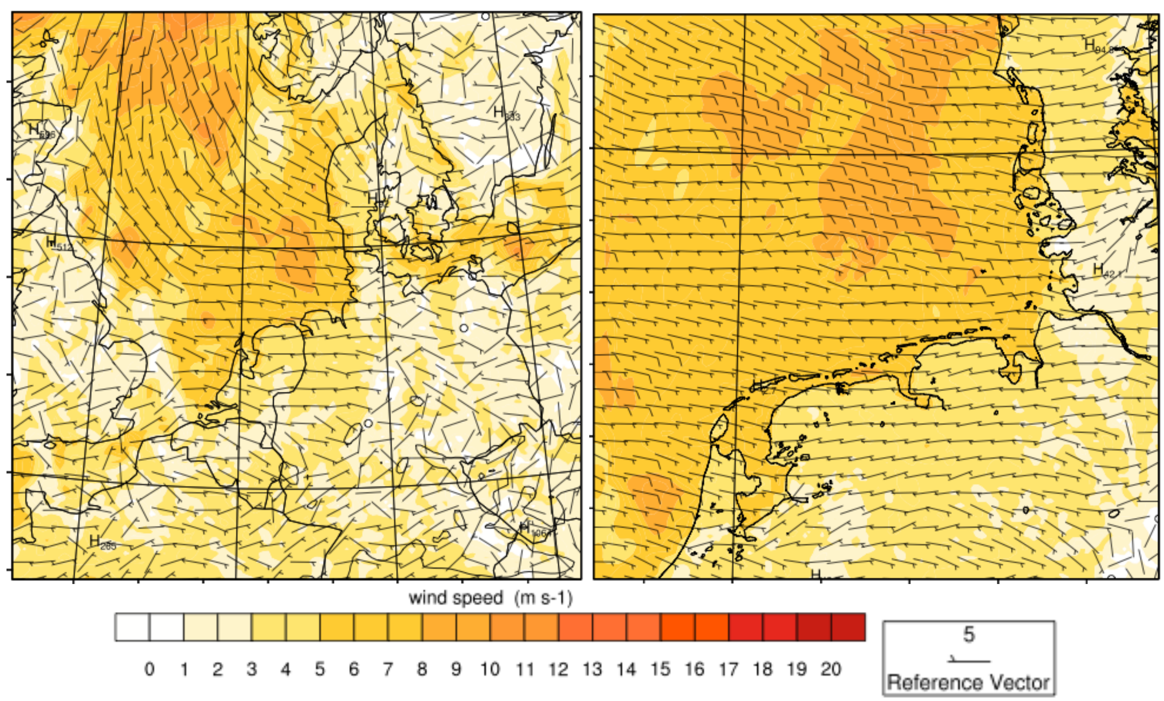

Figure 2.3 10-m winds for WRF domain 2 (left) and 3 (right) at 01z on July 2, 2006.

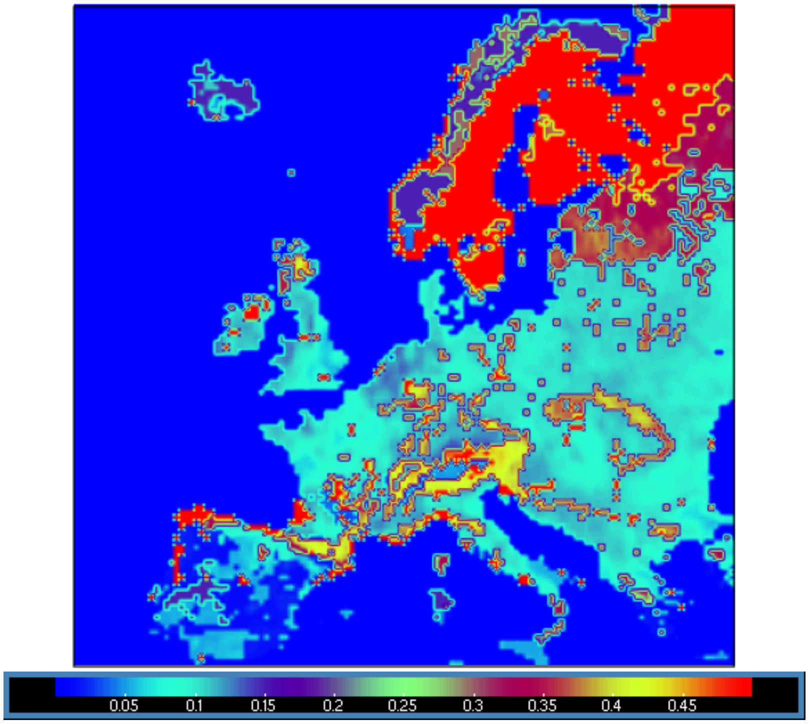

Figure 2.4 WRF roughness length without coupling on domain 1 at 01z on July 2, 2006.

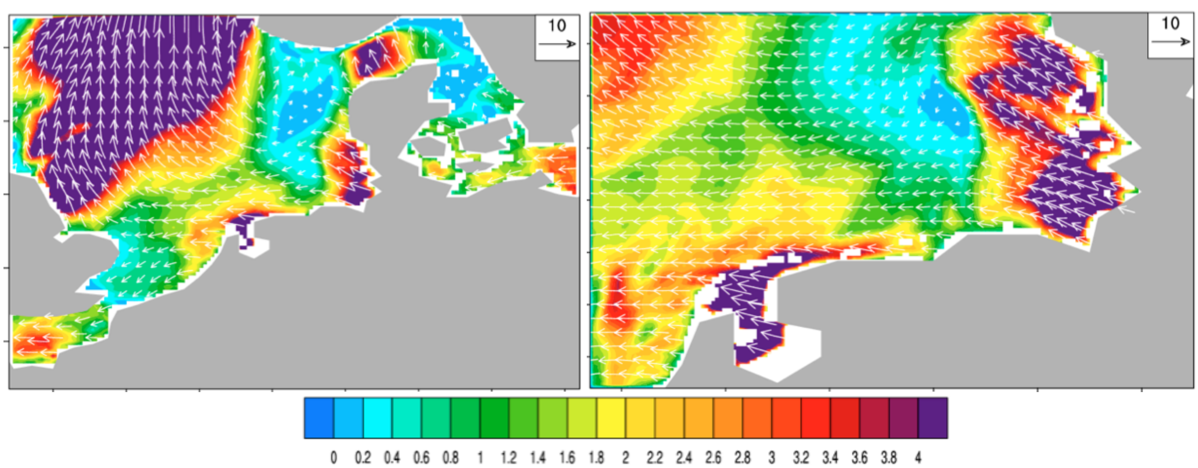

Figure 2.5 WWIII roughness length on domain 2 (left panel) and on domain 3 (right panel) at 01z on July 2, 2006. Roughness length in in meter and was scaled by 10^5.

3. State Estimation (SE) Experiments with WRF SCM/DART

In this section the state estimation (SE) experiments in 1D and 3D are described. The goal is to use data assimilation to improve predictions of winds in the lower part of the MBL, which are relevant to off-shore wind energy applications. This is accomplished by using state estimation to improve the estimate of key parameters of the BL parameterization, which in turn result in better initial conditions and short-term forecasts over water.

3.1 WRF-FDDA 3D runs

The WRF model version 3.4.1 was set up over Northern Europe centered over the FINO 1 platform, to provide lateral forcing for the Single Column Model (SCM) experiments. These mesoscale runs are performed with NCAR's FDDA, which has been extensively tested over the years and is known to provide a good fit with the available observations. The assimilated observations were from the World Meteorological Organization (WMO) Global Telecommunications Service (GTS) database (http://www.wmo.int/pages/prog/www/TEM/index_en.html). Those are worldwide observations made available in real-time by NOAA. The observations that were assimilated in those experiments include radiosondes, surface stations, buoys, ships, and aircraft reports. Figure 3.1 shows the location of the platform (54° 00' 53.5"N, 6° 35' 15.5"E) over the WRF computational grids configuration. There are three nested domains with, respectively, 30 km, 10 km and 3.3 km grid increment, with 132x132/41 grid points. There are 41 vertical levels, with eight levels in the first 500 m above the sea at approximately: 15 m, 45 m, 75 m, 100 m, 130 m, 195 m, 315 m and 490 m. No feedback to coarser domains was allowed (i.e., one-way nesting).

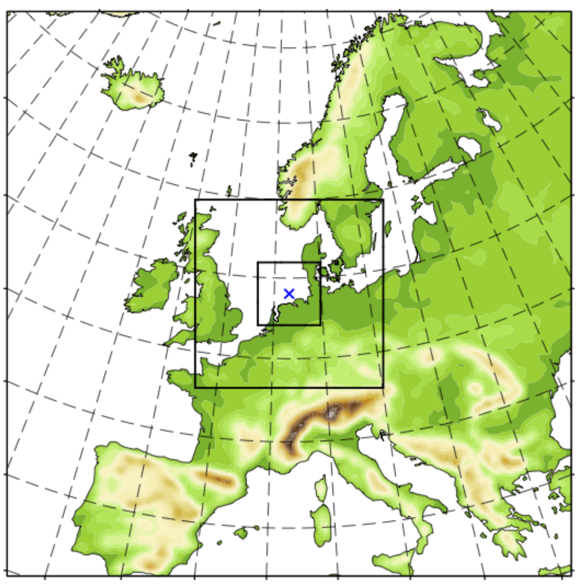

Figure 3.1 WRF domains configuration centered over the FINO 1 tower location (blue cross). The grid size increment is 30 km, 10 km and 3.3 km.

The physical parameterization follows Draxl et al. (2012). This is a configuration developed for North Sea applications by the Department of Wind Energy of Technical University of Denmark.

These physics options included the following: Thompson microphysics scheme, Kain–Fritsch cumulus parameterization (domains 1 and 2 only), sixth-order numerical diffusion, and positive definite advection of moisture and scalars. The rapid radiative transfer model and Dudhia schemes are used for longwave and shortwave radiation calculations, respectively. The 2.5-level Nakanishi and Niino (2006) PBL's surface layer scheme (MYNN) scheme was selected. The model is initialized with global data from the NOAA's Climate Forecast System Reanalysis (CFSR) project (Saha et al. 2010). The CFSR data are 6-hourly global reanalyses at 0.5° grid increment valid from 1979 to 2010. The 6-hourly data are also used for lateral boundary conditions along the largest domain. In addition, daily sea surface temperature data from the NCEP's OISST project are used. The OISST data are provided at 1/4° grid increment between 2001 and 2005, and 1/12° thereafter. Where available over the North Sea and North Atlantic, SST analyses from the Danish Meteorological Institute (DMI), which are at higher resolution than the OISST data, are used, and the DMI SST product (www.myocean.eu) is blended with the NCEP OISST product near the DMI dataset's outer boundary. Land use categories come from MODIS.

Figure 3.2 shows an example of the 80-m winds as estimated by WRF at four different times on 25 Dec 2006. The shading indicates the wind speed while the wind vectors are indicated by wind barbs. The sequence indicates a closed circulation developing to the north west of the domain (06 UTC), then progressively moving towards the north of the FINO tower that is indicated by the blue cross (12 and 18 UTC). This is an example of the complexity of the hub-height wind field at these locations, which may result in significant shifts of both wind speed and direction over a relative short span of time.

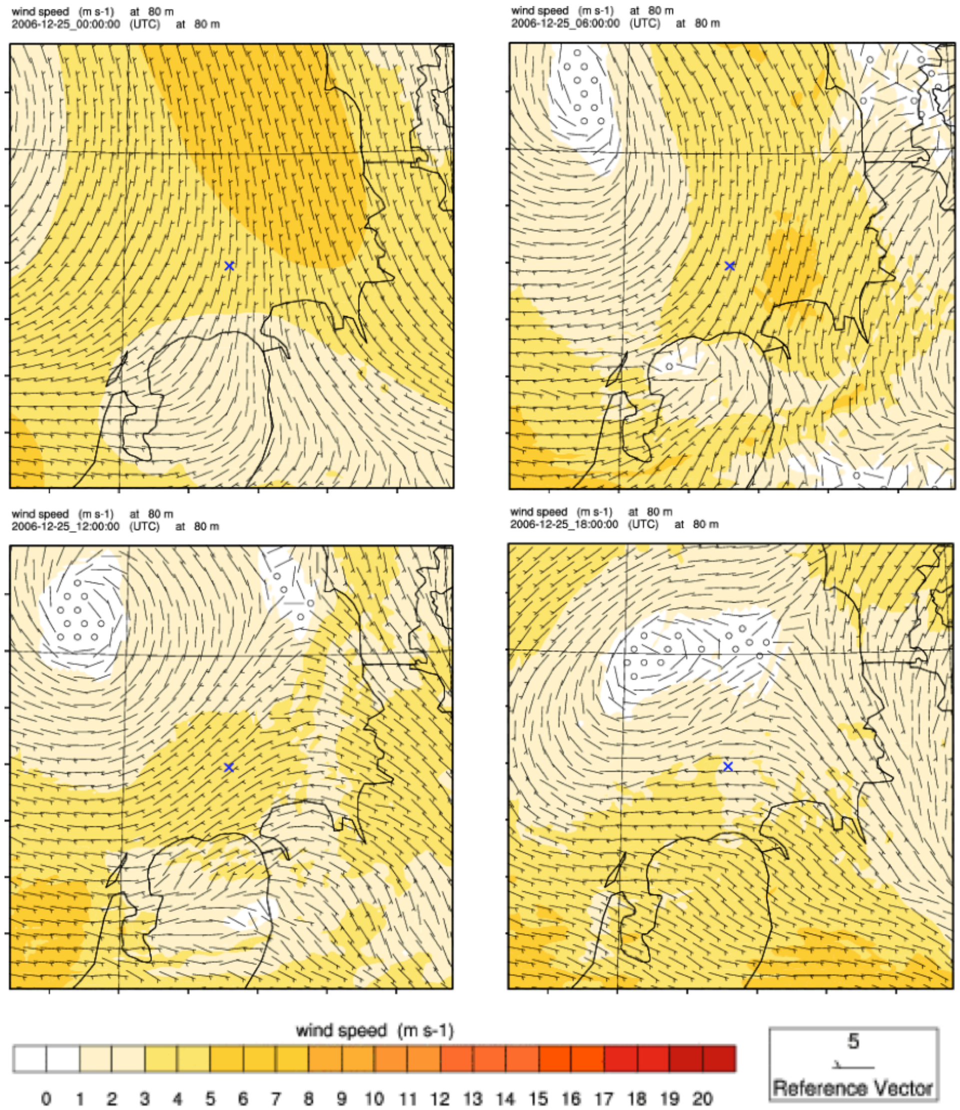

Figure 3.2 WRF 80-m wind on Dec. 25, 2006 at 00, 06, 12, and 18 UTC (Δx = 3.3 km).

Figure 3.3 shows the probability density function (PDF) of wind speeds at several heights and over the October-December 2006 period of observations and WRF estimates at the FINO 1 tower. The model does a good job at reconstructing the observed PDF, which is relevant for off-shore wind resource assessment applications.

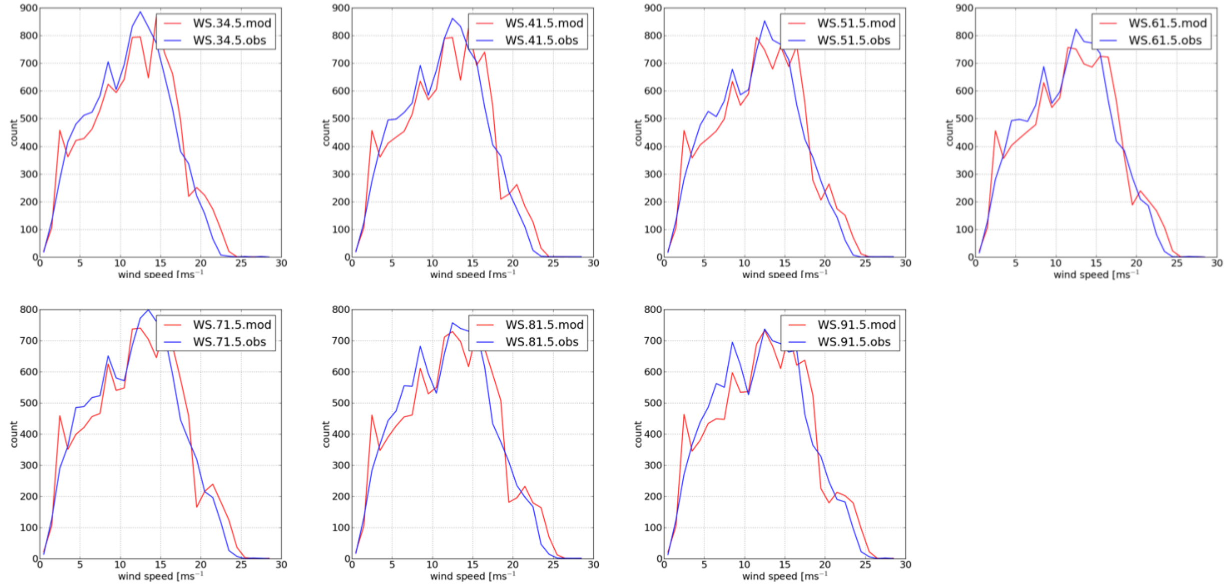

Figure 3.3 Probability density functions of wind speed of the WRF estimates (red) and FINO 1 observations (blue) at several heights and over the October-December 2006 period.

The following are the runs that have been completed with WRF 3D to generate a set of lateral forcing for WRF SCM:

- October – December 2006 WRF 3D runs with global SST are complete;
- October – December 2006 WRF 3D runs with local SST from DMI are complete (used as forcing for “Baseline” SCM experiments in Sec. 3.2);
- October – December 2006 WRF 3D runs with local SST from DMI and the assimilation of WMO observations are complete (used as forcing for “FDDA” SCM experiments in Sec. 3.2);

These runs are archived on NCAR's mass storage system, and will be made available to interested individuals and groups.

3.2 WRF SCM-DART ensemble runs

Prior to converting the FINO1 observations to DART format, additional processing and quality control was required. For wind speed observations, the concern was primarily due to “mast shadowing” effects, where the tower mast influences the wind speed observations recorded by anemometers. Due to engineering and structural stability limitations, the anemometer booms on offshore towers like FINO1 are much shorter than they typically are on land-based towers, and thus the mast shadowing effect cannot be ignored for FINO1 wind speed observations. The wind speed observations that are affected by mast shadowing must either be corrected in some fashion, or assigned a large quality control flag so that they are effectively withheld from the data assimilation process.

At each of the seven wind observation heights on the FINO1 tower (34 m, 41 m, 51 m, 61 m, 71 m, 81 m, and 91 m), the anemometer boom is mounted on the southeast side of the tower, while the wind vane boom is mounted on the northwest side of the tower. The boom angles vary slightly by height. For each observation height we defined the anemometer observation to be shadowed when the winds came from the direction (Anemometer boom angle) + 180° +/- 30°. DART requires that observations be decomposed into zonal (U) and meridional (V) wind components as well, so for valid observations we required that a wind speed and wind direction pair be present; if either was missing, we assigned the U and V observations missing values.

To examine what percentage of the FINO1 wind observations from 1 Oct – 31 Dec 2006 were either shadowed or missing, for each 10-minute observation time we tallied the number of levels with valid wind speed/direction pairs. Figure 3.4 shows this information as a function of time, and Figure 3.5 tallies the total counts of valid observations at each level throughout the three months. We note that there are at most six valid levels of wind observations because the 61-m wind vane was offline during these three months, and the 41-m wind vane was also offline from 6 Dec 2006 onward. From Figs. 3.4 and 3.5 we see that only 13.7% of the observation times have no valid wind observations, while over 80% have either five or six valid levels of wind observations. We also calculate how many periods for which there are no valid wind observations, as well as their duration. Figure 3.6 shows that while there are a few wind data "outages" that last half a day or a day, the vast majority are one hour or less in duration. We assimilated observations into the SCM-DART system hourly, and so the impact of these data outages was minimal. Therefore, because we have at least one valid wind observation over 86% of the time, and because most of the periods without valid wind observations are short, we chose to effectively withhold the shadowed wind observations from the assimilation system by assigning them a large quality control flag.

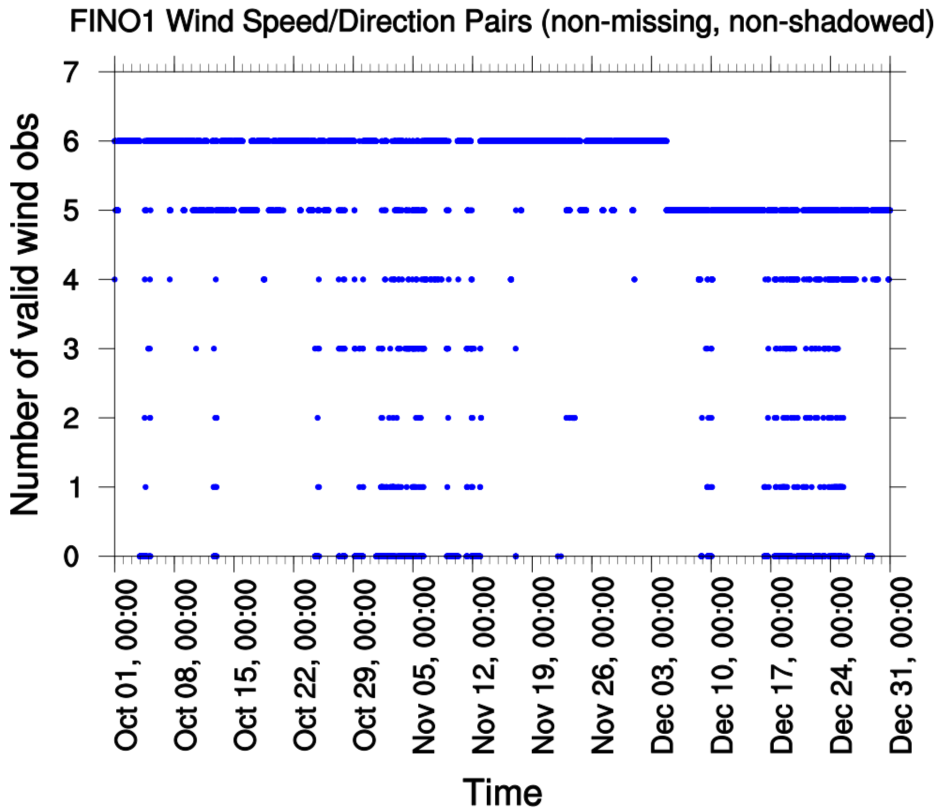

Figure 3.4 For the period of 1 Oct – 31 Dec 2006, each blue dot represents how many of the seven levels on the FINO1 tower have valid (non-missing and non-shadowed) wind speed/direction observation pairs for each 10-minute observation time.

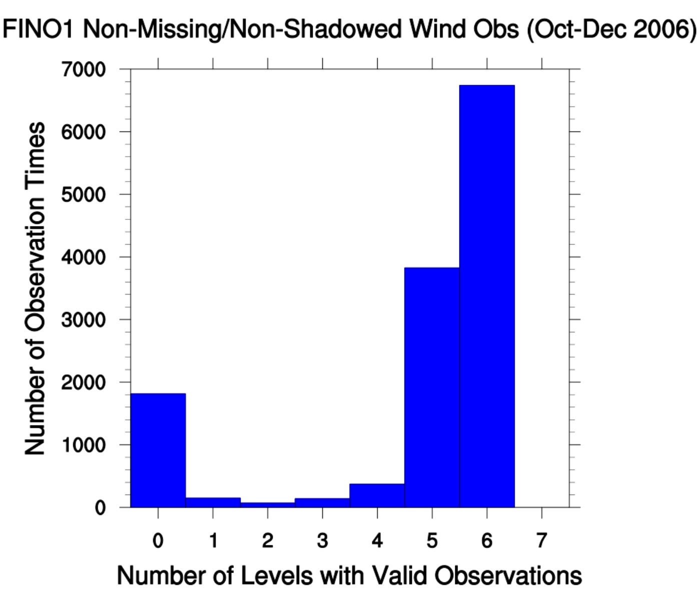

Figure 3.5 Bar chart indicating the number of 10-minute observation times from 1 Oct – 31 Dec 2006 for which there are a given number of levels with valid (non-missing, non-shadowed) wind speed/direction observation pairs.

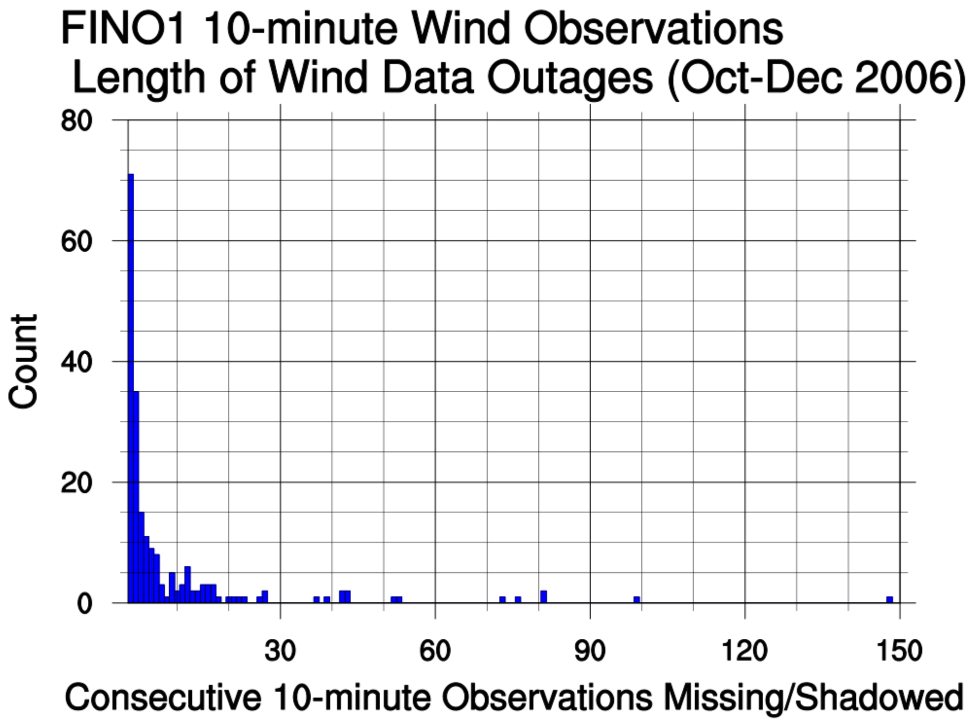

Figure 3.6 Count of the number of consecutive 10-minute observations from 1 Oct – 31 Dec 2006 for which all FINO1 wind observations are either missing or shadowed.

In order to use the WRF SCM for this project, we modified the version of the code that is distributed to the community. We modified WRF SCM to allow users to specify a set of eta levels in the WRF namelist, rather than allowing the model to generate its own set of eta levels based on a specified number of vertical levels (in this project we used 10 levels from 30 m to 210 m with 20-m intervals, and 50 levels above 210 m.) We also modified WRF SCM to work either over land or over water based on the actual land use categories read in from the 3D WRF output files that drive the SCM simulation (the community version of WRF-SCM is hard-wired to run over land only). Another modification we made is for the SCM to use SST for subsurface initialization if the SCM point is over water. These improvements and modifications to the SCM code will be made available to the community in an upcoming release of WRF.

We developed a scripting system and the optimal settings to run the WRF SCM-DART experiments. The main features of this configuration are:

- 1-hour data assimilation cycling;
- The selected ensemble Kalman filter (EnKF) algorithm in DART is based on the Ensemble adjustment Kalman filter (EAKF, Anderson 2001);

- Assimilation of the FINO 1 observations (available across multiple levels) of U- and V-wind components, temperature, and dew point temperature;
- 100-member ensemble for EnKF calculations (performed within the DART software);
- Lateral forcings ("boundary conditions") produced with mean forcing from the WRF 3D runs and ensemble perturbations derived by empirical orthogonal functions (EOFs) of each relevant variable from WRF 3D output; these perturbations' magnitude roughly matches the RMSE of the 3D WRF for the time period selected, to assure statistical consistency of the lateral information driving the SCM;
- The perturbations are a linear combination of the first several EOFs, whose coefficients are random numbers constrained by an auto-regressive process, to ensure temporal consistency;
- Vertical localization of the EnKF algorithm has been set to 4 km after several sensitivity tests.

The new scripting system and the optimal settings to run the WRF SCM that were identified above were used to perform the 1D experiments with WRF SCM. Moreover, state estimation experiments were performed with the goal of further improving the results. Specifically, the value of a key parameter was estimated with the WRF SCM-DART system, allowing the available observations to influence the chosen parameter values at every time step. Tests were performed to find parameters suitable for such experiments. Although several parameters in the boundary layer and surface layer schemes were considered, we focused our attention on the time-varying roughness length. Charnock-determined roughness length (which is in the WRF model and several other state-of-the-science numerical weather prediction models) is known to be poorly estimated over water in strong winds, especially in shallow (~30 m depth) water where offshore wind turbines are often located (similar to FINO 1 conditions). As shown by Jimenez and Dudhia (2014), the Charnock roughness length can be 2-3 orders of magnitude too small in strong wind conditions.

Figure 3.7 shows an example of the sensitivity of lower level winds (i.e., the average across the FINO 1 tower) to the roughness length values. On the left, there is the baseline run with the Charnock's formulation available in WRF, whereas on the right is shown a run with a fixed value of the roughness length (0.1 m), which is about two orders of magnitude higher than the baseline value. Shown are both the predicted (red) and observed (blue) wind speed. Clearly the roughness length has a strong influence on low-level winds, and the Charnock formulation does not seem to reproduce the observed values for a large portion of the period examined.

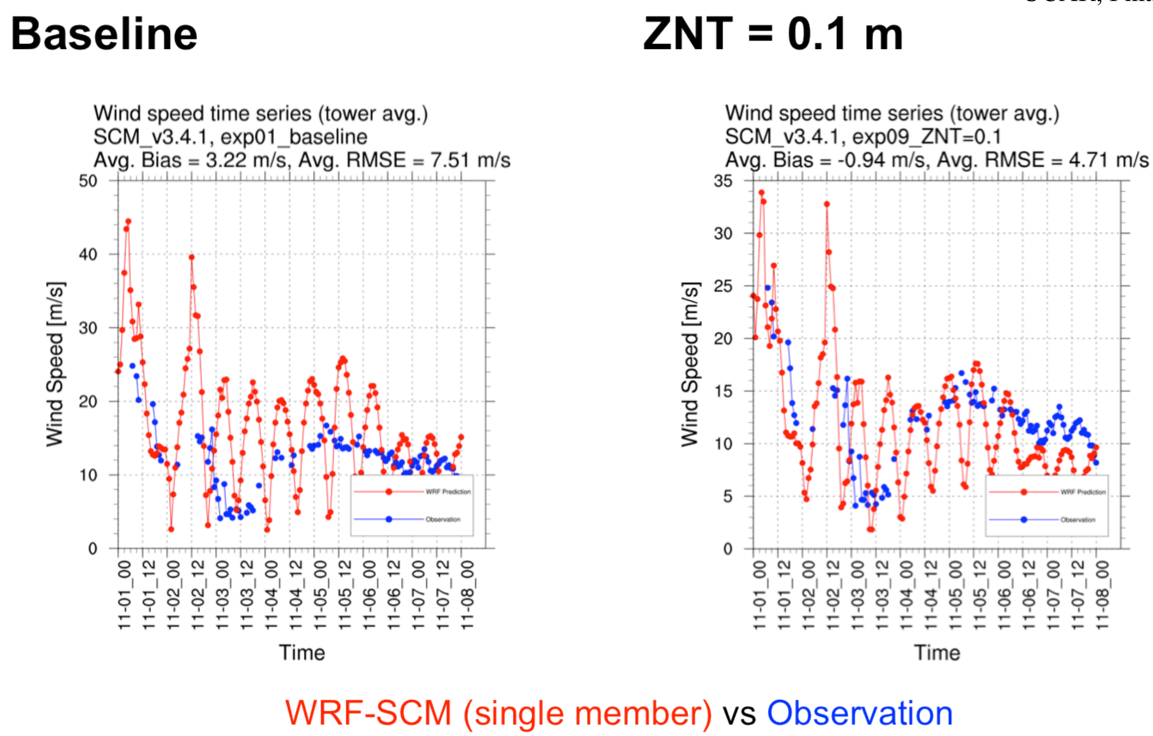

Figure 3.7 Free WRF SCM simulations (i.e., without data assimilation) with the baseline Charnock's formulation available in WRF (left) and with a constant roughness length value of 0.1 m (right), for the first week of November 2006.

The following runs were performed with the WRF SCM-DART system, using WRF version 3.5.1 and modifications to both WRF and DART that allow state estimation of the time-varying surface roughness length Z_0:

(1) **"Baseline"**: October – December 2006 SCM runs with forcing with 3D WRF without DA;
(2) **"Baseline+ZNT_est"**: October – December 2006 SCM runs with forcing with 3D WRF without DA and with Z_0 estimated with DART.
(3) **"FDDA"**:October – December 2006 SCM runs with forcing with 3D FDDA WRF;
(4) **"FDDA+ZNT_est"**: October – December 2006 SCM runs with forcing with 3D FDDA WRF and with Z_0 estimated with DART.

Examples of a monthly time series of SCM-DART ensemble mean 1-h forecasts of wind speed and temperature at FINO1 compared against observations and the 3D WRF simulation that drove the SCM-DART ensemble are shown in Figs. 3.8-9. These figures are from the FDDA+ZNT_est experiment for the month of Nov 2006. For the wind speed plot in Fig. 3.8, the 1-h ensemble mean forecasts (red) are on average of similar accuracy as the 3D WRF wind speed at FINO1 (black), and the model predictions track the observations reasonably well. For the temperature plot in Fig. 3.9, the ensemble mean forecasts closely match the observations and have smaller errors than the 3D WRF run. Because the only forcing to the SCM was provided by geostrophic winds, it was expected that the SCM-DART system would remain closer to the temperature observations than to the wind speed observations, and these figures confirm that expectation.

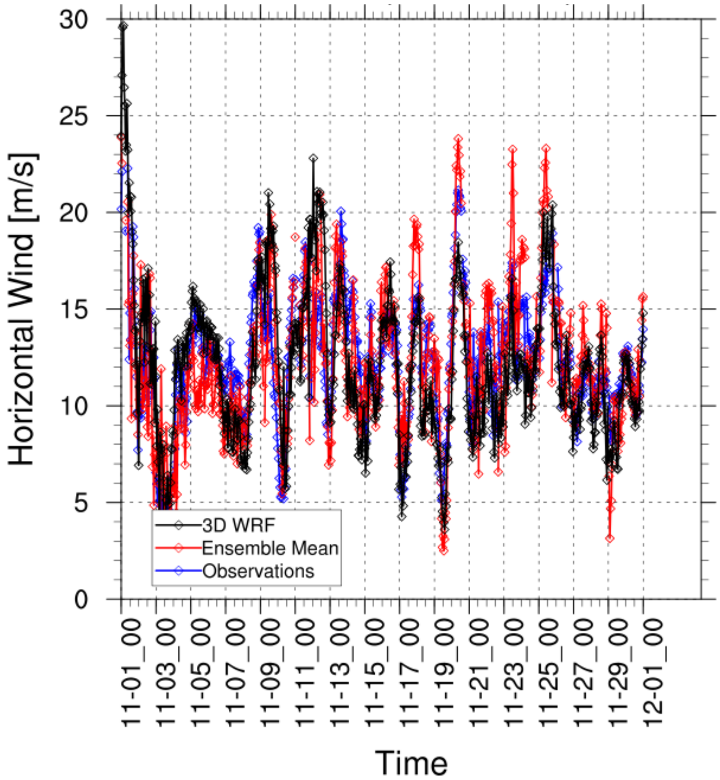

Figure 3.8 Time series of wind speed forecasts and observations (blue) at the FINO1 tower, averaged over the tower depth, for the FDDA+ZNT_est experiment for Nov 2006. The SCM-DART ensemble mean 1-h forecasts are in red, and this experiment's corresponding 3D WRF prediction at FINO1 is in black.

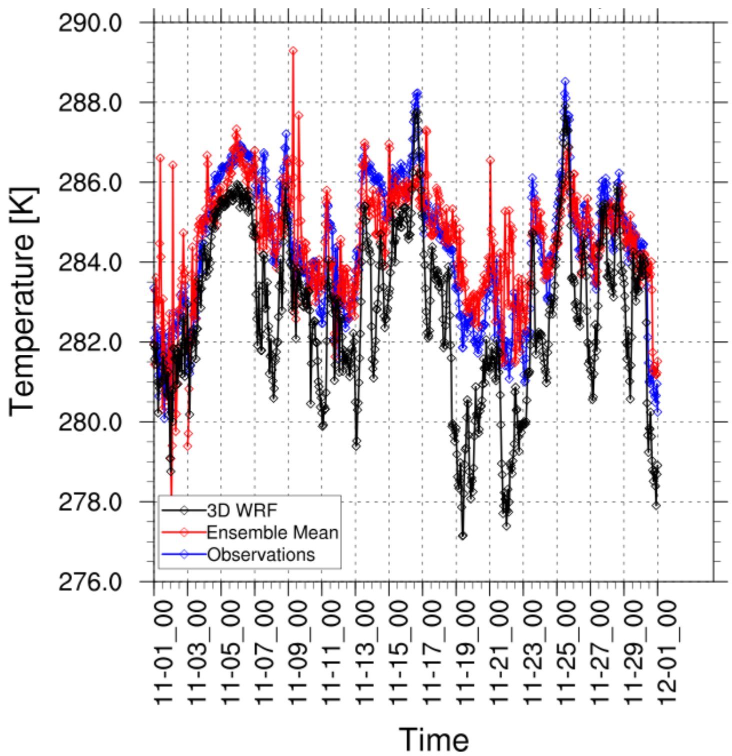

Figure 3.9 As in Fig. 3.8, but for temperature.

Performance metrics for the four SCM-DART experiments described above are shown in Fig. 3.10-12 for wind speed, U, and V, respectively. For the month of October, the results reflect the initial hypothesis, i.e., both the higher-quality boundary conditions and the estimation with data assimilation of a key parameter, the surface roughness Z_0, improved the wind estimates at the FINO 1 tower. The best results are obtained when both approaches are combined, and the largest improvements results from the Z_0 estimation. These improvements result primarily in a lower bias (the systematic component of RMSE), with very little change in the centered RMSE (CRMSE; the random portion of RMSE). In all cases the correlation between the prediction of observations is preserved, which is a desirable feature while also generating an overall significant reduction of RMSE. However, for November and December the impact of the forcing provided with the WRF 3D runs with data assimilation did not consistently result in improvements based on the shown metrics, while the Z_0 estimation always results in an improvement. Similar results (not shown) where obtained for other variables (e.g., temperature and dew point temperature).

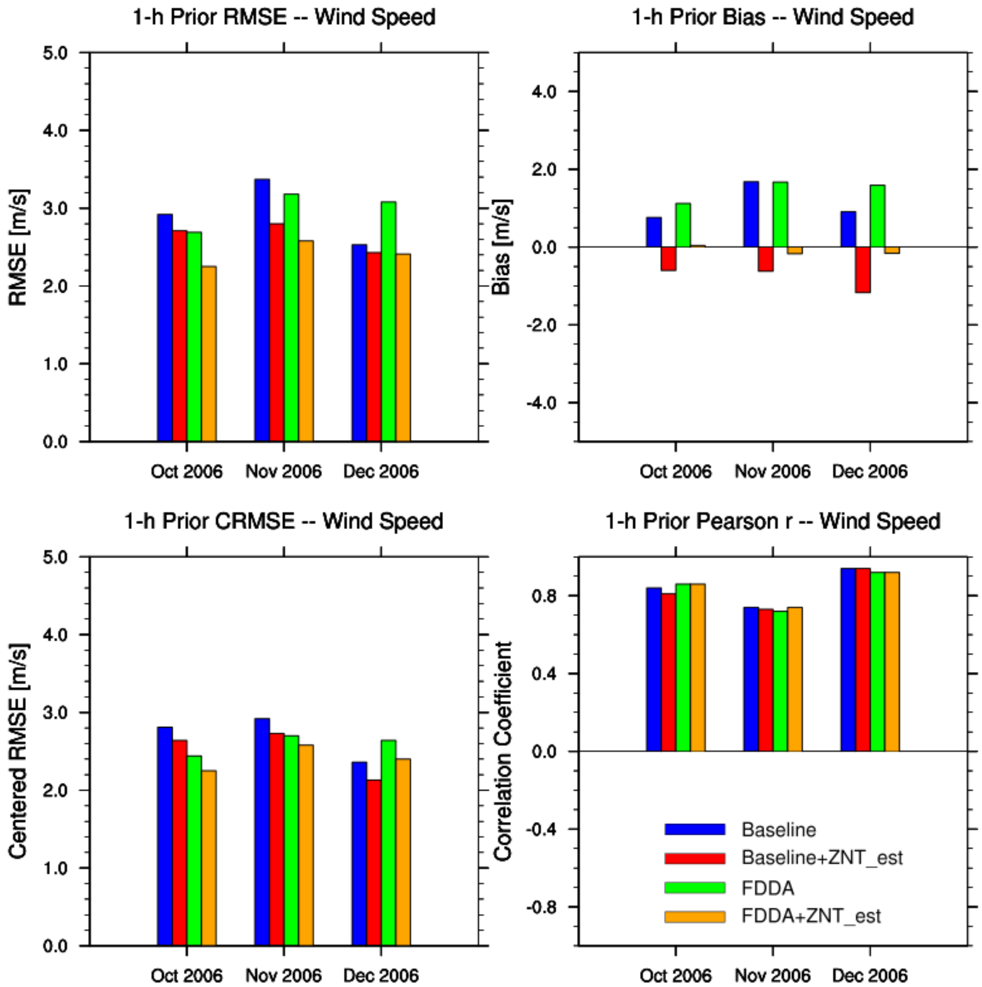

Figure 3.10 Root mean squared error (RMSE; top-left), bias (top-right), centered RMSE (bottom-left), and correlation (bottom-right) of 1-h wind speed predictions for the month of October, November and December 2006. Shown are values for the Baseline (blue), Baseline+ZNT_est (red), FDDA (green), and FDDA+ZNT_est (orange) experiments. See main text for description of the four experiments.

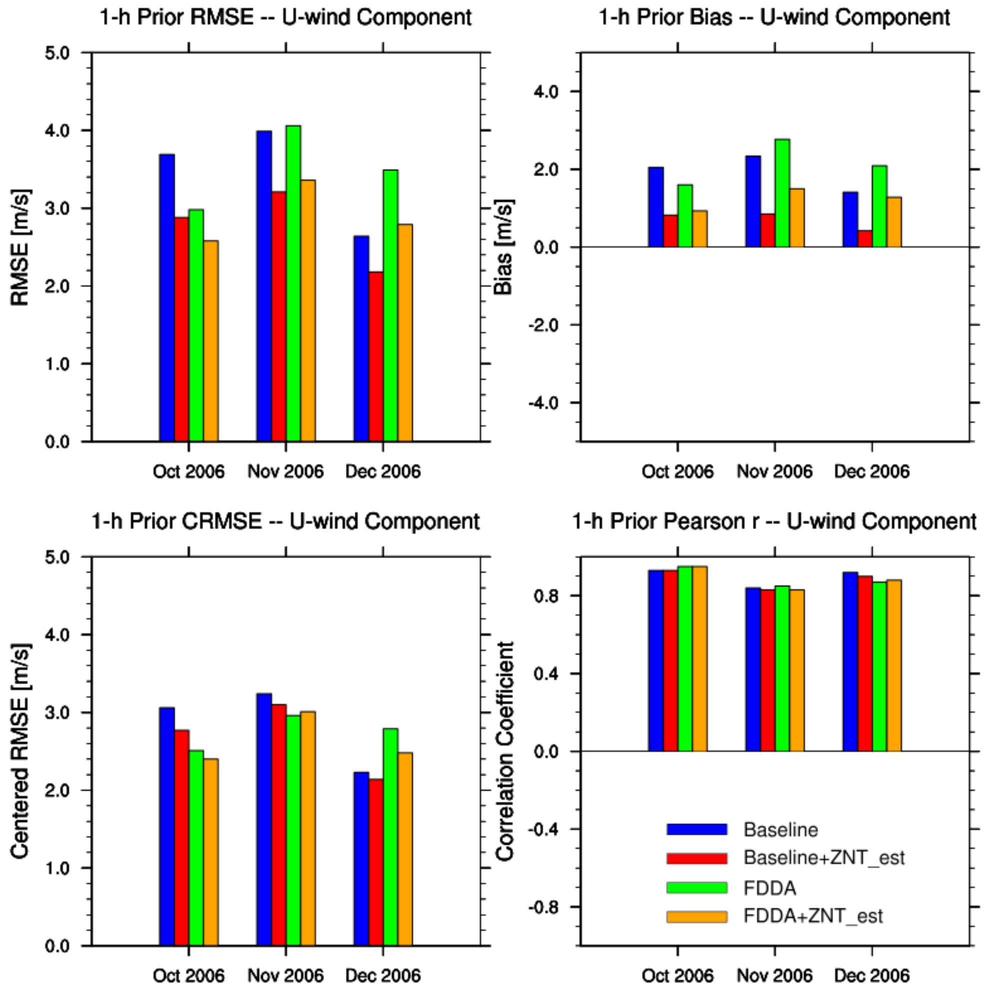

Figure 3.11 Same as in Fig. 3.10, but for the zonal wind component (U).

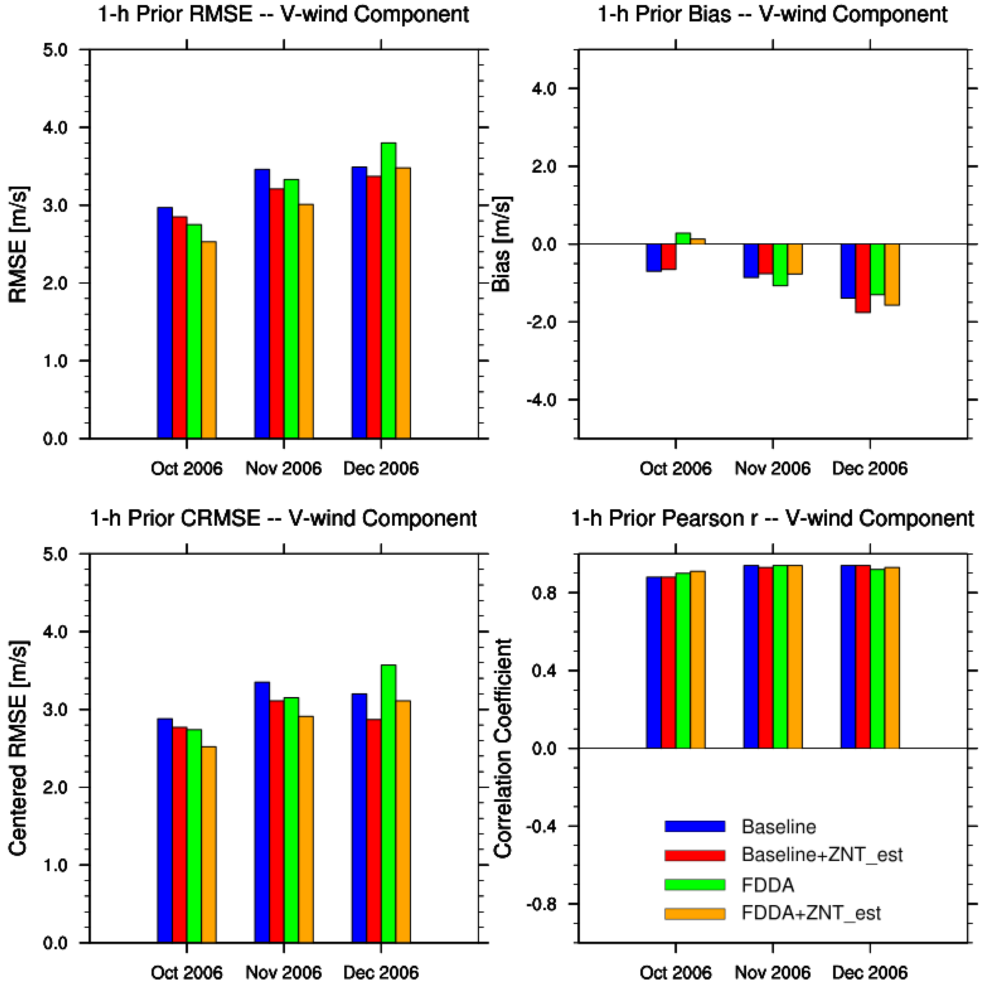

Figure 3.12 Same as in Fig.3.10, but for the meridional wind component (V).

Figure 3.13 shows an analysis of the same experiments presented in Figs. 3.10-12, but by looking at the vertical profile of the different metrics at FINO 1, with the addition of total spread, which when matched with the RMSE of the ensemble mean provides and indication of the ability of the probabilistic prediction system to quantify the prediction uncertainty, which is a key factor to support cost-effective decision making. Results are shown for the east-west component (U) and the month of October. Similar results were obtained for the north-south component (V) and wind speed, and the months of November and December (not shown). Also shown is the number of available observations across the different vertical levels (cyan) and the assimilated observations (purple).

The first aspect to notice is the limited vertical variability of the metrics, which makes the analysis shown in Figs. 3.10-12 based on averages across the tower representative of the whole column. Also, as evident from Fig. 3.13, no wind component data is available at 61 m because of the 61-m wind vane being non-operational during the last half of 2006. The lowest bias is obtained when the forcing are provided with the WRF 3D runs with data assimilation (right column). The lowest RMSE is shown in the bottom-right panel, which correspond to the run where the WRF 3D runs with data assimilation provide the forcing, and Z_0 is estimated with the

WRF SCM / DART system. An overall reduction of the centered RMSE can also be observed, although not as large as the improvements shown in the bias results. All the tested systems shows a good relationship between the total spread and the RMSE, with perhaps the best results shown once again in the bottom-right panel.

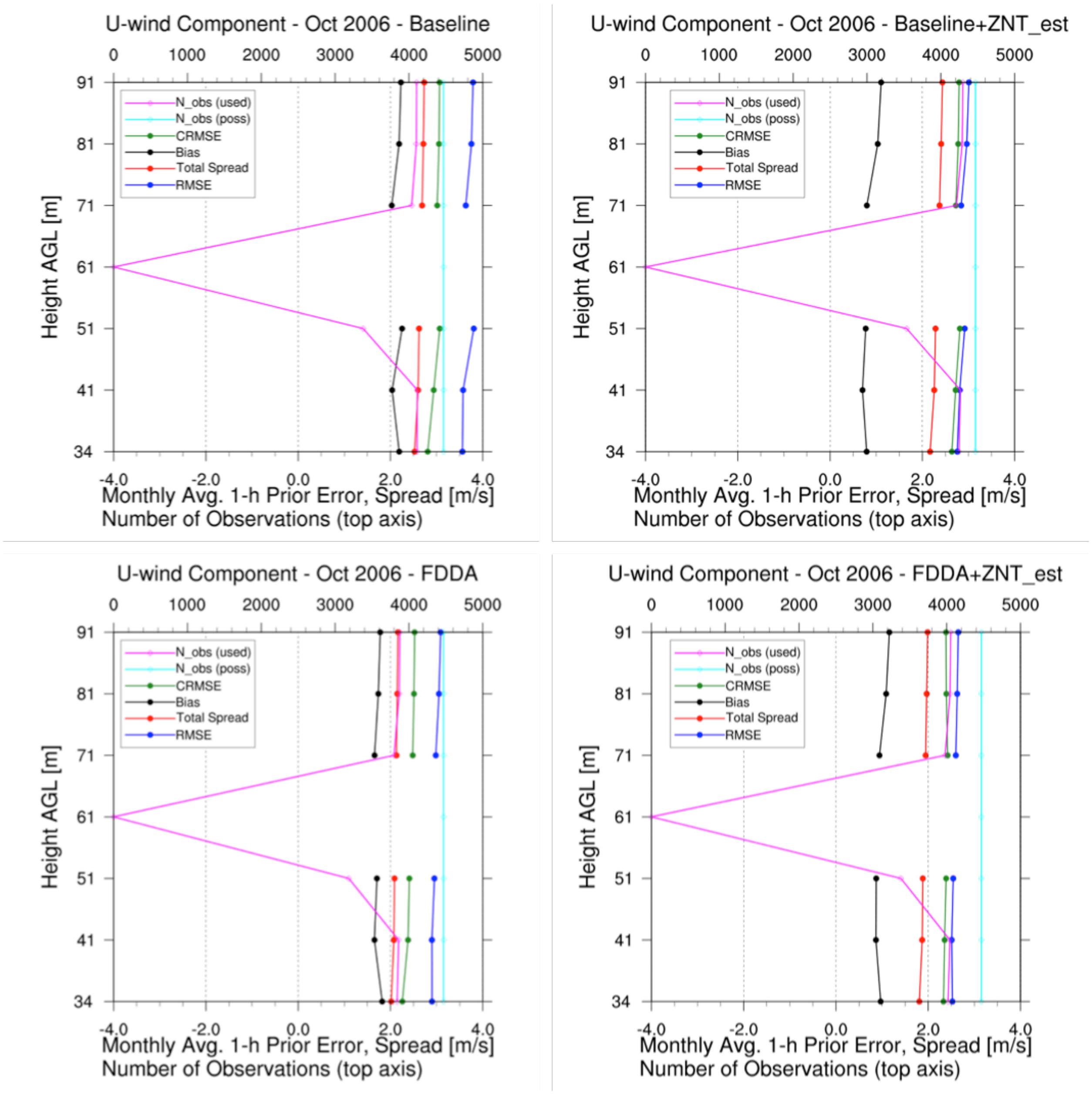

Figure 3.13 Vertical profiles at FINO 1 of Root mean squared error (RMSE; blue), bias (black), centered RMSE (green), total spread (red), number of available observations (cyan), and assimilated observations (purple). Shown values are for 1-h predictions of east-west wind component (u) for the month of October, and for the WRF SCM /DART baseline run (top-left), WRF SCM /DART run including the Z_0 estimation (top-right), WRF 3D runs with Four Dimensional Data Assimilation (FDDA; bottom-left), and WRF SCM /DART run including the Z_0 estimation using as forcing the WRF 3D runs with FDDA (bottom-right).

Based on the overall reduction in RMSE that we saw in our experiments in the runs where DART estimated Z_0, we thought it was important to dig a little deeper and examine the boundary layer turbulent stresses in these experiments. To do that we had to re-run all the SCM-DART experiments with a WRF namelist option turned on to output the turbulence budget terms every hour, from which the turbulent stresses could be derived and calculated. We compared these modeled stresses to observed stresses from Sonic anemometers on the FINO1 tower, located at heights of 40 m and 80 m. The observed stresses were provided by Javier Sanz-Rodrigo, who is an external collaborator on other NCAR projects. Figure 3.14 shows the same statistics as Fig. 3.10 did, but for the turbulent stress <uw> at 40 m, with a time series of the stresses in Fig. 3.15.

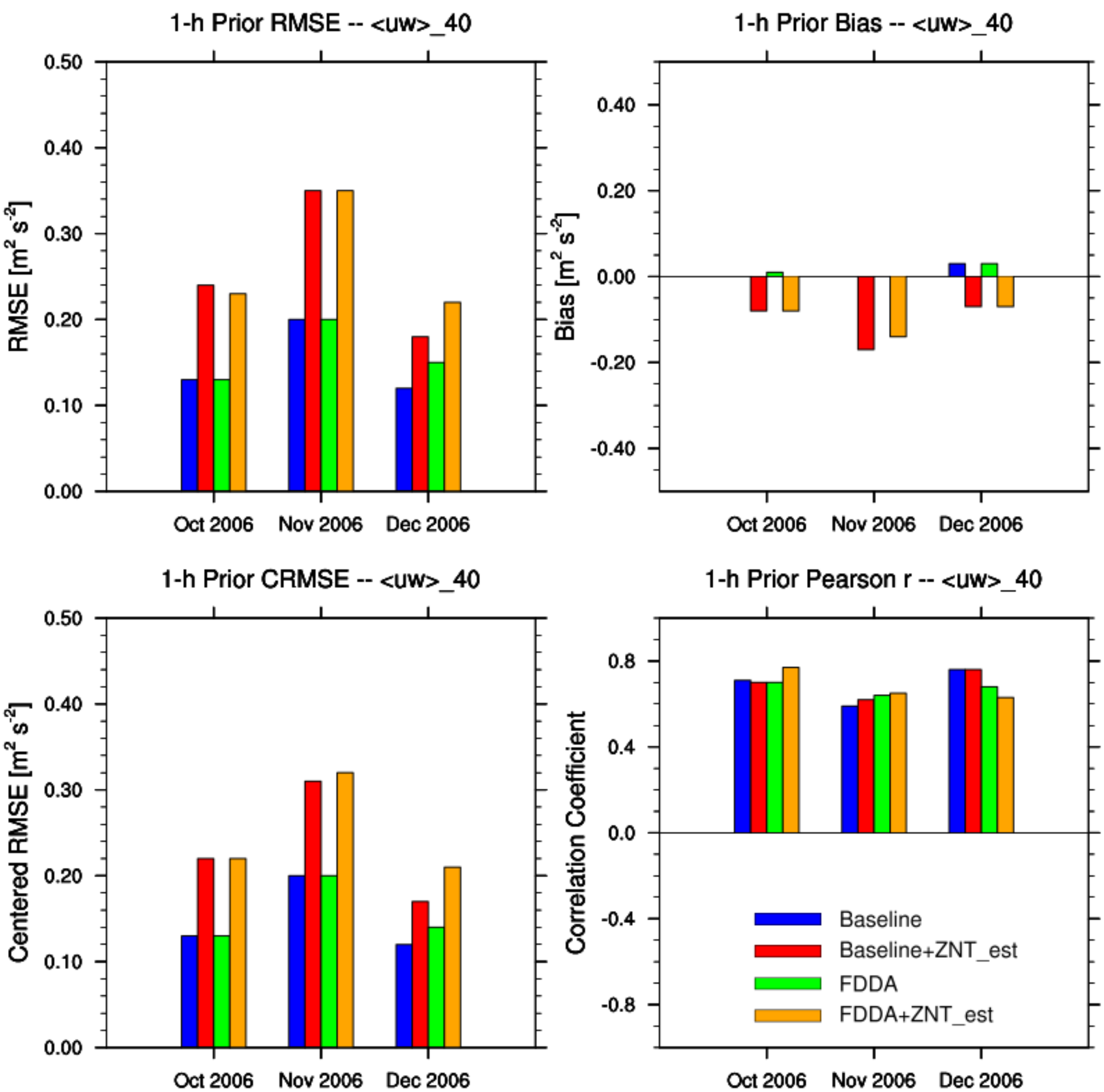

Figure 3.14 Same as Fig. 3.10, but for turbulent stress <uw> at 40 m.

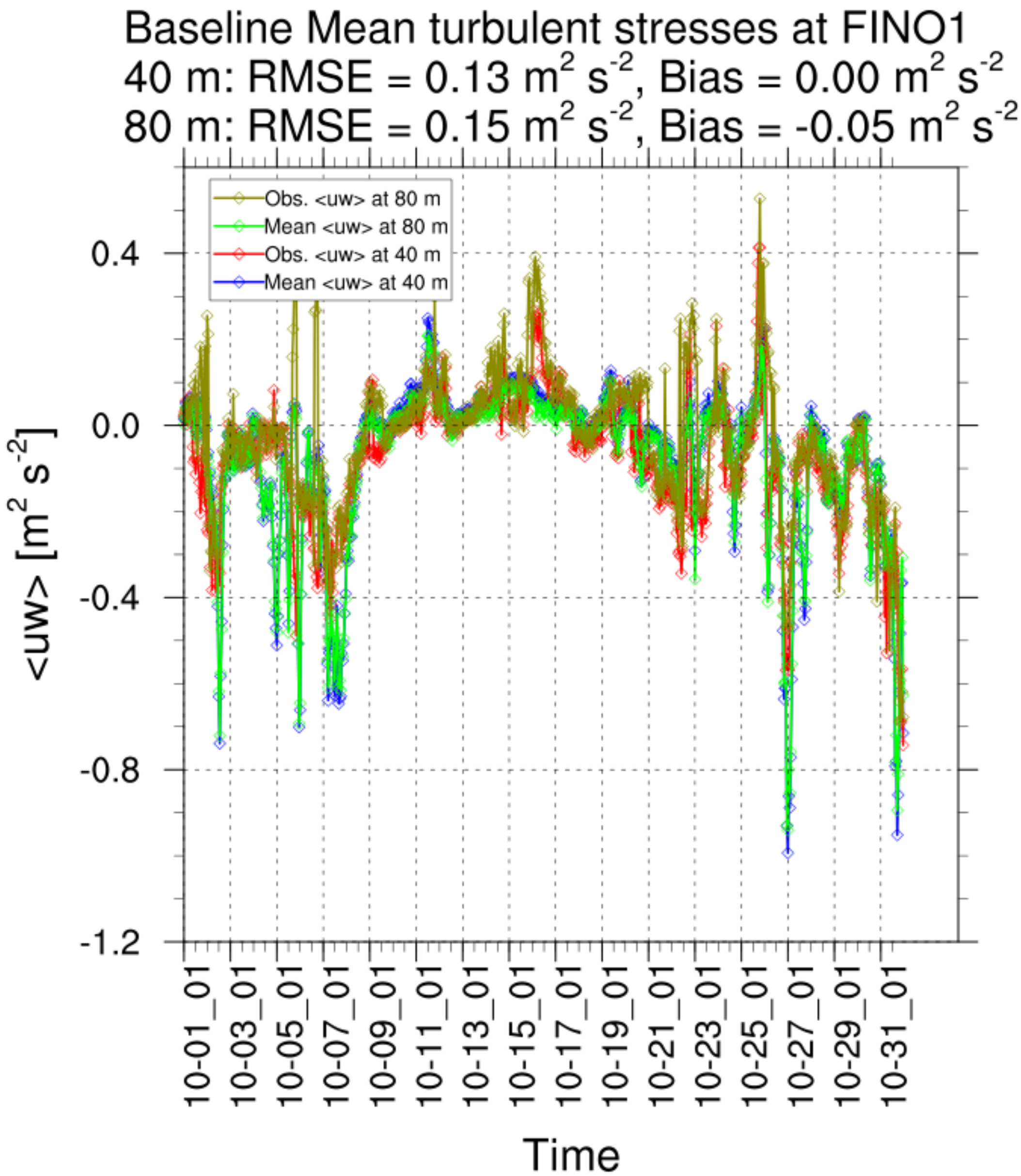

Figure 3.15 Time series of the turbulent stress <uw> during Oct 2006 SCM-DART Baseline experiment. Model-derived ensemble-mean stresses are in blue (40 m) and green (80 m), with observed stresses in red (40 m) and dark yellow (80 m).

In Fig. 3.14 the RMSE for <uw> is quite low for both experiments that use the Charnock formulation to calculate Z_0 (Baseline and FDDA), with the bias over each month being nearly zero. For both sets of forcings, the RMSE, CRMSE, and bias were larger for the experiments where DART estimated Z_0 than those that used the Charnock formulation. Because the errors in the turbulent stress increased with DART estimating Z_0, while wind speed errors decreased in the same experiments, it appears that estimating Z_0 is compensating for errors that come from a source other than the fluxes.

Overall these results confirm one of the key hypotheses of this project, which leads to significant improvements in the estimate of off-shore low-level winds that will impact positively the U.S. off-shore industry. That is, estimating uncertain parameters of NWP boundary layer schemes over water for neutral to unstable conditions within a data assimilation framework leads to significant improvements in wind predictions.

3.3 WRF 3D-DART ensemble runs

As part of this task, the following preliminary steps were performed:

- Diagnosed and solved a stability problem for the ZNT_Charnock (baseline) ensemble;
- Searching for best configuration to use for the ZNT_DART (parameter estimation) ensemble.

After several iterations of testing, the stability problems with the ZNT_Charnock ensemble in the first few simulation days was found to be caused primarily by two factors. The first key factor was the extremely dense surface mesonet observations, which mostly overlapped with areas that already have good coverage from METAR observations. An example of this dense surface observation network is shown in Fig. 3.16. When there are too many observations, the Kalman filter in DART reduces the prior ensemble spread to be artificially small, and the inflation to be artificially large, which often causes stability problems. To address this issue we withheld all the land mesonet observations so that they would only be evaluated (i.e., used for error statistics) but not assimilated.

The second key factor was an observation error threshold that was too high. In DART the observation error threshold is set to a number of standard deviations away from the ensemble mean state. If this threshold is too high, then too many questionable or bad observations get assimilated, which drags the model away from the true state, and creates artificial shocks and increments. In earlier iterations of this testing, it was found that several bad observations were making it through the quality control (QC) step and getting assimilated. Once we reduced the observation error threshold from 3.0 standard deviations to 2.0 standard deviations, these low-quality observations were rightly rejected, and the ensemble became stable.

Once we achieved a stable ZNT_Charnock ensemble for eight model days, we proceeded to tune the observation error variances so that the RMSE roughly equaled the total spread (ensemble spread plus observation error). Wind speed ensemble mean predictions compared against observations are shown in Figs. 3.17 and 3.18. In addition to this tuning, we thinned the FINO1 observations so that only observations recorded within 10 minutes either side of the top of the hour were used. We thinned these observations to help preserve ensemble spread.

After we tuned the observation error variances, we transferred the ensemble to our cost-share partners at Vattenfall, and provided them technical support to help them get the ensemble up and running.

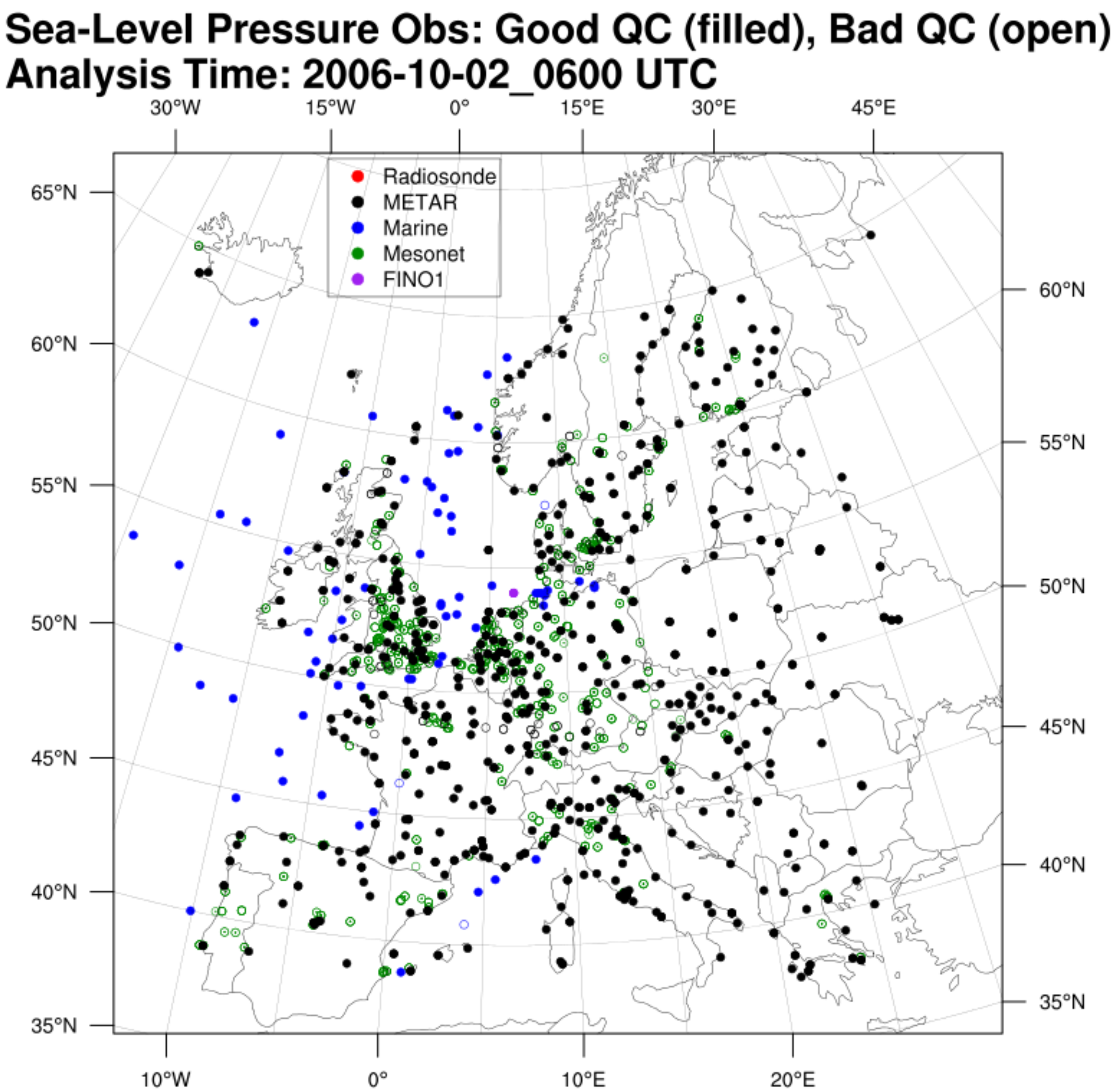

Figure 3.16 Map of locations of sea-level pressure observations at 0600 UTC on 2 Oct 2006 from the METAR (black), marine (blue), land mesonet (green), and FINO1 observations. Filled circles represent observations that passed DART quality control and were assimilated, while open circles represent observations that were not assimilated.

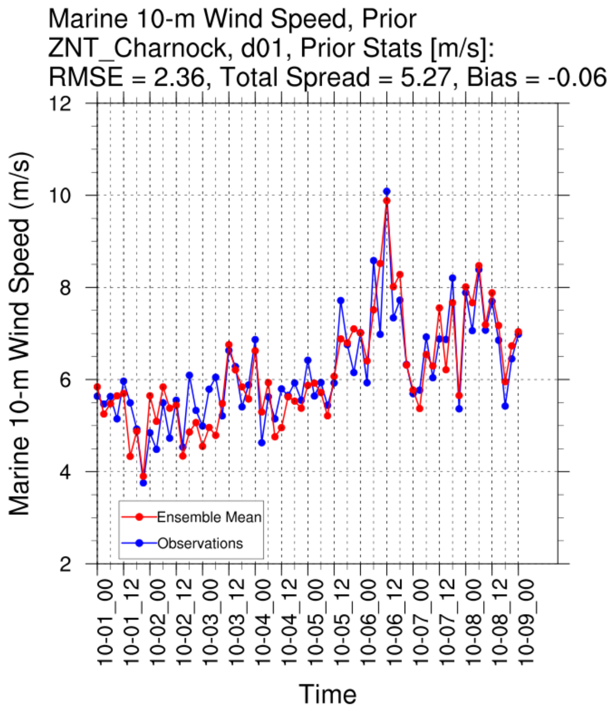

Figure 3.17 Domain-averaged prior ensemble mean wind speed from the ZNT_Charnock ensemble (red) compared against marine buoy wind speed observations (blue).

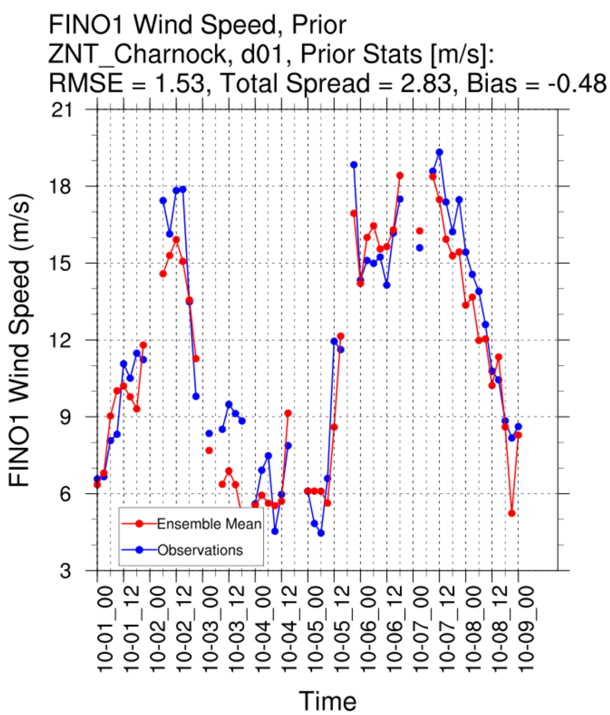

Figure 3.18 Same as Fig. 8, but for FINO1 wind speed observations.

3.3.1 Performance evaluation on WRF 3D/DART runs in the Charnock setup

Vattenfall Wind R&D has been the industrial cost-share partner in this project and has been leading the effort of running the WRF 3D/DART system in a setup with sea surface roughness calculated by the Charnock equation, as follows:

$Z_0 = \propto_c \frac{{U_*}^2}{g}$(Charnock 1955)

The experiment averaged performance statistics

The experiment-averaged RMSE and bias is computed to quantify the average performance of the DART data assimilation effort across the domain and throughout the experiment period. The Dart data assimilation cycle has been run for nearly 1 month and details of the runs are listed in table below.

Table 3.1 Configuration of the WRF 3D/DART runs.

Ensemble members	Update frequency	Horizontal resolution	Area	Verification period
48	3 hours	30 km	Northern Europe	1-29 Oct 2006

The experiment averaged performance metrics (RMSE and bias) are computed by averaging over both time and space and providing a RMSE for each observational platform and each physical variable, providing also the number of observation points that were used to compute the metrics. The metrics are first averaged over the entire domain for each assimilation cycle where useful observations were available and then averaged over the entire period of the experiment to find the experiment-averaged metrics. The following are the steps for calculating the experiment-averaged metrics:

- First, the total error computed as the square of the domain mean RMSE of the model innovations times the number of observation used:

$$TE = Domain\_Mean\_RMSE(y - hx)^2 * Nobs_{used\_epoch}$$

- Second, the total errors and the number of observation used are summed over the experiment period

$$TE_{\_experiment} = \sum_{start-cycle}^{end\_cycle} TE$$

where

$$N\_obs_{used_{experiment}} = \sum_{start-cycle}^{end\ cycle} Nobs_{used\_epoch}$$

- Third, the experiment averaged RMSE is computed as

$$RMSE_{experiment} = \frac{TE_{experiment}}{Nobs_{experiment}}$$

Only observations with DART quality control values between 0-3 were used to compute the metrics and quality control values between (4-7) were rejected. The meaning of the dart quality codes are listed in Table 3.2 below:

Table 3.2 Dart Quality code.

QC flag	Meaning
0	Observation assimilated
1	Observation evaluated only
2	Assimilated, but the posterior forward operator fail
3	Evaluated only, but the posterior forward operator failed
4	l prior forward operator failed
5	Not used because of namelist control
6	Prior QC rejected
7	Outlier rejected

Table 3.3 Experiment-averaged performance metrics: A clear improvement is seen for all variables and across all platforms, where the posterior RMSE is reduced compared to the prior RMSE.

Assimilated and verified Variables	Prior RMSE	Prior Bias	Post. RMSE	Post. Bias	Obs. used
METAR_U_10m	2.73	0.04	2.59	0.03	120413
METAR_V_10m	2.71	-0.39	2.57	-0.38	120677
METAR_TEMP 2m	1.43	-0.26	1.30	-0.24	140179
METAR_DEWP 2m	1.35	-0.41	1.25	-0.36	134742
LAND_SFC_U	2.70	-0.03	2.61	-0.03	234178
LAND_SFC_V	2.66	-0.11	2.58	-0.12	234542
LAND_SFC_TEMP	1.54	-0.32	1.48	-0.30	247272
LAND_SFC_DEWP	1.35	-0.24	1.32	-0.20	221355
LAND_SFC_ALTI	1.53	0.32	1.34	0.25	211037
Fino1_TEM	0.88	-0.71	0.76	-0.60	2686
Fino1_MSLP	1.05	-0.34	0.58	-0.39	568
Fino1_U_WIND	1.93	0.64	1.07	0.21	3309
Fino1_V_WIND	1.94	-0.44	1.11	-0.32	3172
Fino1_horiz WIND	2.72	-0.49	1.53	-0.44	2860
RADIOSONDE_U_	2.27	-0.28	1.49	-0.12	828
RADIOSONDE_V	2.19	-0.15	1.48	-0.10	829
RADIOSONDE_TEMP	1.19	-0.23	1.06	-0.19	1534
RADIOSONDE_DEW	1.38	-0.26	1.27	-0.18	1451
RADIOSONDE_mslp	1.43	0.01	1.09	-0.21	1425

ACARS_U	2.85	0.00	2.46	0.00	11456
ACARS_V	2.87	-0.18	2.46	-0.22	11863
ACARS_TEMP	1.20	-0.09	1.08	-0.05	21268
MARINE_SFC_U	3.84	-0.01	3.56	-0.00	7071
MARINE_SFC_V	3.73	-0.53	3.45	-0.48	7466

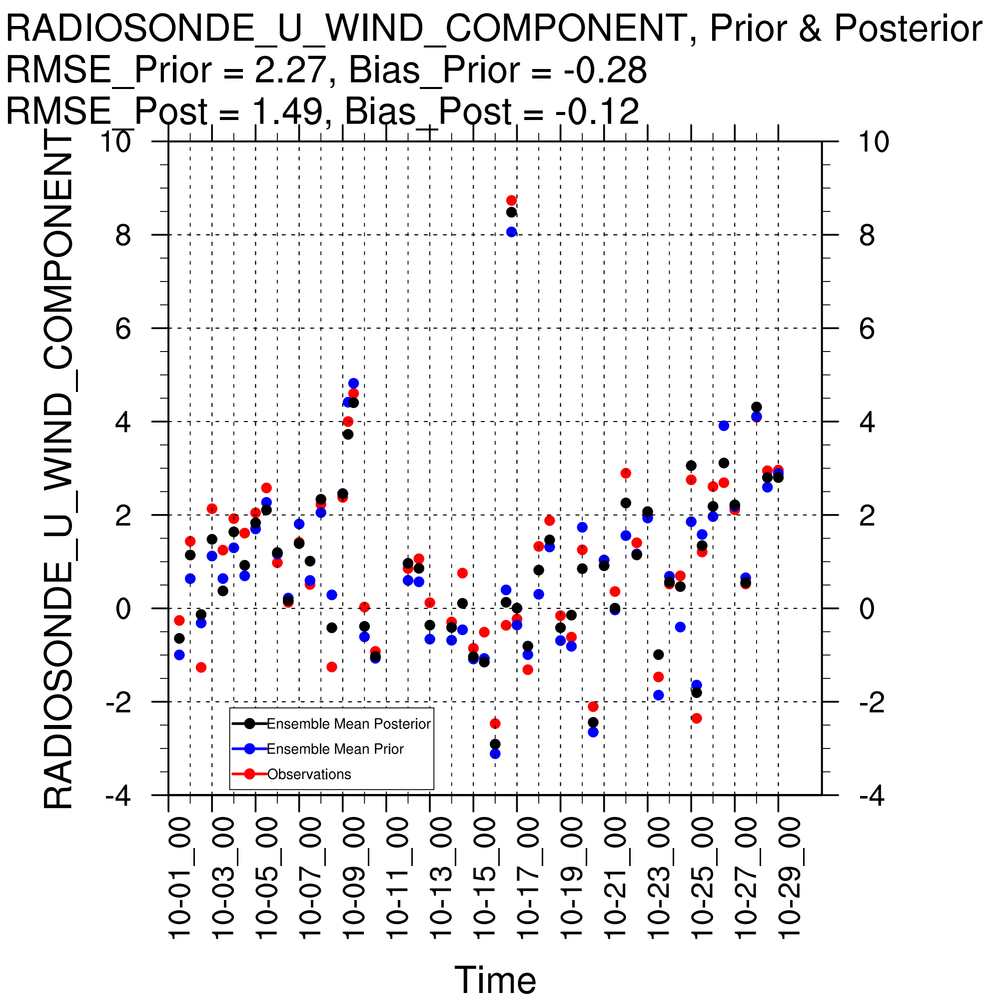

Figure 3.19 Shows domain-averaged model prediction of the radiosonde u component, calculated as the mean of the prior ensemble members (blue dots), and the mean of the posterior ensemble members (black dots), where the red dots are the domain-averaged verifying observations. A clear improvement is seen across the test period as the black dots are pushed away from the blue dots and closer to the verifying observation.

As shown in Figure 3.19 after the SE step (black dots) the model estimates are much closer to the observations (red dots) than before it (blue dots). Along with the results presented in Table 3.3, it is clear that the assimilation procedure based on the DART code that was tested extensively with the single column model (see section 3.2), performs well also with the 3D configuration of the

WRF model. The assimilation of in-situ data appears to be highly beneficial for off-shore wind energy applications, and the resulting increase in accuracy predictions will support an increasing penetration of off-shore wind in the energy market.

Summary and Conclusions

In this project we have improved numerical weather prediction analyses and forecasts of low level winds in the marine boundary layer. This has been accomplished with the following tools:

- The National Center for Atmospheric Research (NCAR) Weather and Research Forecasting model, WRF, both in his single column (SCM) and three-dimensional (3D) versions;
- The National Oceanic and Atmospheric Administration (NOAA) Wave Watch III (WWIII);
- SE algorithms from the Data Assimilation Research Testbed (DART, Anderson et al. 2009);
- Observations of key quantities of the lower MBL, including temperature and winds at multiple levels above the sea surface.

The experiments with the WRF SCM / DART system have lead to large improvements with respect to a standard WRF configuration, which is currently commonly used by the wind energy industry. The single column model appears to be a tool particularly suitable for off-shore wind energy applications given its accuracy, the ability to quantify uncertainty, and the minimal computational resource requirements.

In situations where the impact of an upwind wind park may be of interest in a downwind location, a 3D approach may be more suitable. We have demonstrated that with the WRF 3D / DART system the accuracy of wind predictions (and other meteorological parameters) can be improved over a 3D computational domain, and not only at specific locations.

All the scripting systems developed in this project (i.e., to run WRF SCM / DART, WRF 3D / DART, and the coupling between WRF and WWIII) and the several modifications and upgrades made to the WRF SCM model will be shared with the broader community.

PRODUCTS / DELIVERABLES

The following are the new software, scripts, and data that have been generated in this quarter and that will be shared with the community:

- Scripts to run the WRF SCM system and DART to assimilate the available observations and to estimate the surface roughness length, which results in improved wind predictions for off-shore wind energy applications (section 3.2).
- Scripts to run the WRF 3D system and DART to assimilate the available observations and to, which results in improved wind predictions for off-shore wind energy applications (section 3.3).
- Scripts to run the atmosphere-wave fully-coupled modeling system based on the WRF and WWIII models (section 2).

PARTICIPANTS & OTHER COLLABORATING ORGANIZATIONS

Individuals:

- Dr. Andrew Clifton (NREL, Co-PI): Tasks 1 and 5 lead, funded by this award.
- Dr. Luca Delle Monache (NCAR, PI): project managing, planning and coordination of task activities, funded by this award.
- Dr. Josh Hacker (NCAR, Co-PI): Tasks 3 and 6 lead, providing scientific oversight of the overall project, funded by this award.
- Dr. Sam Hawkins (Vattenfall, Co-I): Tasks 3 and 6 investigator, international collaborator (UK), cost-sharing partner.
- Dr. Branko Kosovic (NCAR, Co-I): Tasks 3 and 6 investigator, funded by this award.
- Dr. Jared Lee (NCAR, Co-I): Tasks 3 and 6 investigator, funded by this award.
- Dr. Jesper Nissen (Vattenfall, Co-I): Tasks 3 and 6 investigator, international collaborator (Denmark), cost-sharing partner.
- Dorita Rostkier-Edelstein (IIBR, Co-I): Tasks 3 and 6 investigator, international collaborator (Israel), unfunded.
- Dr. Francois Vandenberghe (NCAR, Co-PI): Tasks 2 and 5 lead, funded by this award.
- Dr. Yonghui Wu (NCAR, Co-I): Tasks 2 and 5 investigator, funded by this award.

Organizations:

- National Center for Atmospheric Research (NCAR, lead institution), Boulder, CO.
- National Renewable Energy Laboratory (NREL), Golden, CO.
- Vattenfall, Stockholm, Sweden.
- Israel Institute for Biological Research (IIBR), Ness-Ziona, Israel.

CHANGES / PROBLEMS

None.

BUDGETARY INFORMATION

See attached tables.

Bibliography

Andreas, E., L. Mahrt, and D. Vickers, 2014: An Improved Bulk Air-Sea Surface Flux Algorithm Including Spray-Mediated Transfer. Accepted for publication in *Quart. J. Royal Meteorol. Soc.*.

Anderson, J. L., 2001: An ensemble adjustment Kalman filter for data assimilation, *Mon. Wea. Rev.*, 129, 2884–2903.

Donelan, M. A., F. W. Dobson, S. D. Smith, and R. J. Anderson, 1993: On the dependence of sea surface roughness on wave development. *J. Phys. Oceanogr.,* **23**, 2143–2149.

Draxl C., A. Hahmann, A. Pena and G. Giebel, 2012: Evaluating winds and vertical wind shear from Weather Research and Forecasting model forecasts using seven planetary boundary layer schemes. *Wind Energy*, DOI: 10.1002/we.1555.

Edson, J., and C. V. Fairall, 1998: Similarity relationships in the marine atmospheric surface layer for terms in the TKE and scalar variance budgets. *J. Atmos. Sci.*, **55**, 2311–2328.

Edson, J., and Coauthors, 2007: The coupled boundary layers and air–sea transfer experiment in low winds. *Bull. Amer. Meteor. Soc*., **88**, 341–356.

Geernaert, G. L., K. B. Katsaros, and K. Richter, 1986: Variation of the drag coefficient and its dependence on sea state. *J. Geophys. Res.,* **91**, 4762–4779.

Hacker, J., and D. Rostkier-Edelstein, 2007: PBL state estimation with surface observations, a column model, and an ensemble Kalman filter. *Mon. Wea. Rev.*, **135**, 2958–2972.

Hanley, K. E., and S. E. Belcher, 2008: Wave-driven wind jets in the marine atmospheric boundary layer. *J. Atmos. Sci.*, **65**, 2646–2660.

Hare, J. E., T. Hara, J. B. Edson, and J. Wilczak, 1997: A similarity analysis of the structure of air flow over surface waves, *J. Phys. Oceanogr.,* **27**, 1018–1037.

Hwang, 2011: A note on the ocean surface roughness spectrum. *J. Atmos. Ocean. Tech*., **28,** 436-443.

Izumi, Y., 1971: Kansas 1968 field program data report. Air Force Cambridge Res. Lab. AFCRL-72-0041, Environ. Res. Paper No. 379, Hanscom AFB, MA, 79 pp.

Janssen, P. A . E. M., 2004: *The Interaction of Ocean Waves and Wind*. Cambridge University Press, Cambridge, 300+viiipp.

Jimenez, P. A., and J. Dudhia, 2014: Improving the characteristics of the surface roughness over shallow waters. 15th Annual WRF Users' Workshop, Boulder, CO, 24 Jun 2014. Poster. Abstract available at: http://www2.mmm.ucar.edu/wrf/users/workshops/WS2014/abstracts/p7.pdf.

Liu, Y., T.T. Warner, J. F. Bowers, L. P. Carson, F. Chen, C. A. Clough, C. A. Davis, C. H. Egeland, S. Halvorson, T.W. Huck Jr., L. Lachapelle, R.E. Malone, D. L. Rife, R.-S. Sheu, S. P. Swerdlin, and D.S. Weingarten, 2008: The operational mesogamma-scale analysis and forecast system of the U.S. Army Test and Evaluation Command. Part 1: Overview of the modeling system, the forecast products. *J. of Appl. Meteor. Clim.*, **47**, 1077–1092.

Lumley, J. L., and H. A. Panofsky, 1964: *The Structure of Atmospheric Turbulence.* J. Wiley and Sons, 229 pp.

Monin, A. S., and A. M. Obukhov, 1954: Basic laws of turbulent mixing in the surface layer of the atmosphere. *Trudy Geofiz. Inst. Aca. Nauk SSSR,* **24**, 163–187.

Nakanishi M., and H. Niino, 2006: An improved Mellor-Yamada level 3 model: its numerical stability and application to a regional prediction of advecting fog. *Boundary-Layer Meteorol*ogy, **119**, 397–407.

Obukhov, A. M., 1946: Turbulence in an atmosphere with non-uniform temperature. *Trudy Inst. Teoret. Geofiz. Nauk SSSR,* 1, 95– 115 (translation in *Bound.-Layer Meteorol.,* 2, 7–29, 1971).

Pichugina Y. L., R. M. Banta, W. A. Brewer, S. P. Sandberg, and R. M. Hardesty, 2011: Doppler-lidar-based wind-profile measurement system for offshore wind- energy and other marine-boundary-layer applications. Submitted to *J. Appl. Meteor. Climatol.*.

Rieder, K. F., J. A. Smith, and R. A. Weller, 1994: Observed directional characteristics of the wind, wind stress, and surface waves on the open ocean. *J. Geophys. Res.,* **99**, 22 589–22 596.

Saha, S., et al, 2010: The NCEP climate forecast system reanalysis. *Bull. Amer. Meteor. Soc.*, **91**, 1015–1057 (http://dx.doi.org/10.1175/2010Bams3001.2).

Sjöblom, A., and A.-S. Smedman, 2003: Vertical structure in the marine atmospheric boundary layer and its implication for the inertial dissipation method. *Bound.-Layer Meteorol.*, **109**, 1–25.

Smedman, A.-S., X. G. Larsen, U. Högström, 2003: Effect of sea state on the momentum exchange over the sea during neutral conditions. *J. Geophys. Res.*, **108**, doi:10.1029/2002JC001526.

Smedman, A., U. Högström, E. Sahleé, W. M. Drennan, K. K. Kahma, H. Pettersson, and F. Zhang, 2009: Observational study of marine atmospheric boundary layer characteristics during swell. *J. Atmos. Sci.*, **66**, 2747–2763.

Sullivan, P. P., J. B. Edson, T. Hristov, J. C. McWilliams, 2008: Large-eddy simulations and observations of atmospheric marine boundary layers above nonequilibrium surface waves. *J. Atmos. Sci.*, **65**, 1225–1245.

Skamarock, W. C., J. B. Klemp, J. Dudhia, D. O. Gill, D. M. Barker, W. Wang, and J. G. Powers, 2005: A description of the Advanced Research WRF Version 2. NCAR Tech Notes-468+STR.

Tolman H. and D. Chalikov, 1996: Source terms in a third generation wave model. *J. Phys. Oceanogr*., **26**, 2497-2518.

Troitskaya, Y., E. Ezhova, and S. Zilitinkevich, 2013a: Momentum and buoyancy transfer in atmospheric turbulent boundary layer over wavy water surface – Part 1: Harmonic wave. *Nonlin. Processes Geophys.*, **20**, 825–839.

Troitskaya, Y., E. Ezhova, D. Sergeev, A. Kandaurov, G. Baidakov, M. Vdovin, and S. Zilitinkevich, 2013b: Momentum and buoyancy transfer in atmospheric turbulent boundary layer over wavy water surface – Part 2: Wind–wave spectra. *Nonlin. Processes Geophys.*, **20**, 841–856.

Wu J., 1982: Wind Stress Coefficients over Sea Surface from Breeze to Hurricane. *J. Geophys. Res.*, **81**, 9704-9706.

Wyngaard, J. C., 1973: On surface layer turbulence. *Workshop on Micrometeorology,* D. A. Haugen, Ed., Amer. Meteor. Soc., 101–49.

Wyngaard, J. C., 2004: Toward numerical modeling in the “Terra Incognita”. *J. Atmos. Sci.*, **61**, 1816–1826.